https://ntrs.nasa.gov/search.jsp?R=19860014380 2020-03-20T15:43:05+00:00Z

View metadata, citation and similar papers at core.ac.uk

brought to you by CORE

provided by NASA Technical Reports Server

NASA
Technical
Paper
2576

March 1986

NASA-TP-2576 19860014380

Analytical and Numerical Studies of the Thermocapillary Flow in a Uniformly Rotating Floating Zone

William W. Fowlis
and Glyn O. Roberts

LANGLEY RESEARCH CENTER
LIBRARY, NASA
HAMPTON, VIRGINIA

NASA

NASA Technical Paper 2576

1986

Analytical and Numerical Studies of the Thermocapillary Flow in a Uniformly Rotating Floating Zone

William W. Fowlis
George C. Marshall Space Flight Center
Marshall Space Flight Center, Alabama

Glyn O. Roberts
Roberts Associates, Inc.
Vienna, Virginia

National Aeronautics
and Space Administration

**Scientific and Technical
Information Branch**

TABLE OF CONTENTS

Page

I. INTRODUCTION 1

II. FORMULATION 3

2.1 The Model and Governing Equations 3
2.2 Parameter Values 5
2.3 The Cylindrical Geometry Assumptions 5

III. ANALYTICAL SOLUTIONS 7

3.1 Linearization 7
3.2 The Temperature Solution 7
3.3 The Interior Solution 7
3.4 The Leading Order $E^{1/3}$ Sidewall Boundary Layer 8
3.5 The Ekman Layers Associated with the $E^{1/3}$ Layer 9
3.6 The First Order $E^{1/3}$ Sidewall Boundary Layer and the $E^{1/4}$ Sidewall Boundary Layer 10
3.7 The Composite Analytical Solutions 13

IV. NUMERICAL SOLUTIONS 15

4.1 The Numerical Model 15
4.2 Numerical Results 15

V. COMPARISON OF THE ANALYTICAL AND LINEARIZED NUMERICAL RESULTS 22

VI. DISCUSSION OF RESULTS 23

6.1 The Linear Flow 23
6.2 The Nonlinear Flow 25

VII. CONCLUSIONS 25

REFERENCES 27

APPENDIX A – THE LEADING ORDER $E^{1/3}$ SIDEWALL BOUNDARY LAYER 28

APPENDIX B – THE EKMAN LAYERS ASSOCIATED WITH THE $E^{1/3}$ LAYER 30

APPENDIX C – THE FIRST ORDER $E^{1/3}$ SIDEWALL BOUNDARY LAYER 32

APPENDIX D – THE $E^{1/4}$ SIDEWALL BOUNDARY LAYER AND ITS ASSOCIATED EKMAN LAYER 34

APPENDIX E – THE NUMERICAL CODE 37

LIST OF ILLUSTRATIONS

Figure	Title	Page
1.	A schematic drawing of the floating zone system for unidirectional single crystal growth....	1
2.	The simplified floating zone configuration chosen for the present studies................	3
3.	The dimensional analytical solutions for the dependent quantities	13
4.	The dimensional solutions for the linearized numerical problem........................	16
5.	The dimensional solutions for the weakly nonlinear flow	18
6.	The dimensional solutions for the strongly nonlinear flow	20
7.	The dimensional solutions for the strongly nonlinear flow	21
8.	The dimensional solutions for the nonrotating flow and for $\Delta T = 5 \times 10^{-4}$°C............	24

LIST OF TABLES

Table	Title	Page
1.	Physical Properties of Liquid Silicon at 1410°C	6
2.	Dimensions of the Floating Zone and Other Experimental Parameters	6
3.	Dimensionless Parameters	6

TECHNICAL PAPER

ANALYTICAL AND NUMERICAL STUDIES OF THE THERMOCAPILLARY FLOW IN A UNIFORMLY ROTATING FLOATING ZONE

I. INTRODUCTION

The accessibility of the microgravity environment of space by NASA's Space Shuttle has stimulated much research into the processing of materials in low gravity. Processing in such an environment holds potential for the development of higher quality products than can be produced in ground-based laboratories, and for the development of completely new materials. Modern solid-state electronics is based on the properties of high quality crystals and there is substantial evidence for believing that superior crystals can be grown from a melt in the absence of flow in the melt. Reviews describing the effects of convection for several crystal growing systems have been given by Pimputkar and Ostrach [1] and Ostrach [2]. This paper is concerned with the fluid dynamical behavior of the floating zone crystal growing system in low gravity.

The floating zone system for unidirectional single-crystal growth from a low-quality polycrystalline material is shown schematically in Figure 1. The ring heater maintains a liquid floating zone that bridges the gap between the two cylindrical solid crystalline rods. Surface tension at the free melt surface holds the liquid together. The polycrystalline rod is fed into the melt zone where it is melted while the other rod is withdrawn from the melt as a single crystal. Many materials of interest absorb impurities from their container walls and, hence, the great advantage of the floating zone system is that contamination can be reduced or even eliminated.

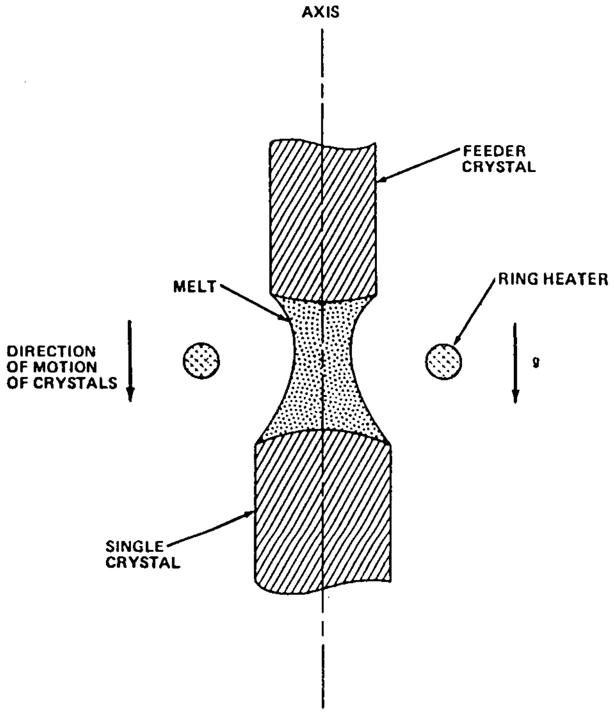

Figure 1. A schematic drawing of the floating zone system for unidirectional single crystal growth. Typical shape distortions are shown for the crystal-melt interfaces and for the free surface in the presence of gravity.

Although crystals of pure substances like silicon are often grown using the floating zone system, there are also many applications of the system where another substance (a dopant) is added to produce a crystal with certain desired properties. Ideally, the dopant should be uniformly distributed throughout the crystal but this is not what is achieved. Variations of dopant concentration in both the radial and axial directions are invariably present [3]. For semiconductors these concentration variations lead to significant variations in electrical conductivity throughout the crystal which substantially degrade the electronic properties for many applications.

The major factors affecting the dopant distribution in the crystal are the temperature and flow fields in the melt. In general, the crystal solidification interface is not flat, and, as a consequence of the differential segregation occurring upon solidification, gravitational buoyancy produces radial concentration variations of the dopant at the crystal interface. Also, radial flows near the crystal interface produce radial dopant variations. Upon solidification these dopant variations lead to dopant variations in the crystal. Time dependent flows lead to striations of dopant concentration variation in the crystal.

Operating a floating zone system in space eliminates buoyant convection, but gravity is not the only driving force for flow in the system. Since surface tension is a function of temperature, the axial temperature distribution produced by the ring heater at the free surface sidewall of the melt drives a thermocapillary (or Marangoni) flow. Thermocapillary flow in a floating zone in the absence of rotation has been the subject of several experimental studies [4,5] (see also Fig. 8 of this paper) and theoretical (numerical) studies [6]. In general, the results show torroidal cells which fully penetrate the melt zone.

The analytical work presented in this paper is an extension of the work by Smith [7] and Smith and Greenspan [8]. These workers examined the idea that the thermocapillary flow could be confined to a thin boundary layer close to the sidewall by means of a uniform rotation of the floating zone about its axis of symmetry. Such a rotation is achieved by rotating the crystals in the same direction at the same rate. Hence, in a rotating system in space there may be effectively no flow in the interior of the melt zone away from the sidewall. Smith [7] and Smith and Greenspan [8] considered a half zone, cold at one end and hot at the other, and tackled analytically the linearized thermocapillary problem in zero gravity and in the absence of crystal growth. They found that the weak, linearized thermocapillary flow is confined to a sidewall boundary layer. To extend this work to more realistic conditions, the present authors considered a full zone, cold at both ends and hot in the interior, and tackled analytically and numerically the linear thermocapillary problem and numerically the nonlinear thermocapillary problem.

In Section II, the model is described, the governing differential equations are presented, and the values chosen for the floating zone dimensions and the other parameters are given. In Section III, linearized, analytical solutions are found using singular perturbation theory and the various sidewall boundary layers described by Greenspan [9] for rotating fluids. In Section IV linear and nonlinear numerical solutions are presented. In Section V the analytical and linearized numerical results are compared, and in Section VI the linear and nonlinear flows are discussed. The conclusions and suggestions for future work are stated in Section VII. Mathematical details of the analytical work and a brief description of the numerical code are given in the Appendices.

Mention should be made of the numerical work on the effects of rotation in a floating zone by Kobayashi and Wilcox [10]. These workers were concerned with the flows driven by differential rotation of the solid endwalls. Thermocapillary driving was not included and hence their work is not relevant to the present paper. Differential rotation of floating zone systems has often been used to mix the melt and to reduce the effects of azimuthal asymmetries of the ring heater. The latter advantage is also present with a uniformly rotating system.

II. FORMULATION

2.1 The Model and Governing Equations

The floating zone geometry is taken to be a right circular cylinder of fluid as shown in Figure 2. The assumptions required for this to be true are discussed in Subsection 2.3. Cylindrical coordinates (r, θ, z) with the z-axis along the axis of symmetry of the fluid cylinder and the origin at the center of the cylinder are used. The top and bottom endwalls of the fluid cylinders are rigid boundaries located at $z = \pm L$. The free surface sidewall of the cylinder is located at $r = a$ and is assumed to be non-deformable (see Subsection 2.3). The endwalls are rotated uniformly with angular velocity, Ω, about the axis of symmetry and are maintained at the melting point temperature, T_m. The sidewall is maintained at $T = T_M + \Delta T \cos \pi z/2L$. This temperature boundary condition is the driving force for the flow. Gravity and the centrifugal force due to rotation are ignored (see Subsection 2.3).

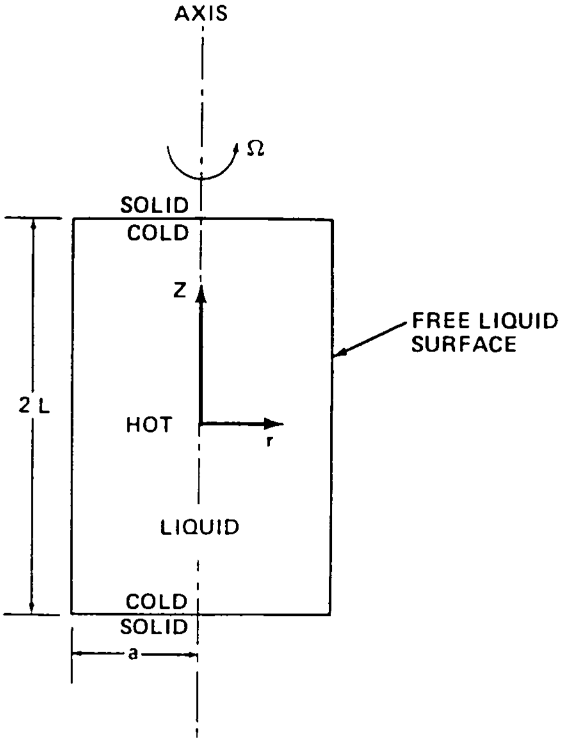

Figure 2. The simplified floating zone configuration chosen for the present studies. The melt is a right circular cylinder of fluid with rigid plane endwalls and a free cylindrical sidewall. Cylindrical coordinates aligned with the axis of symmetry and with the origin at mid-depth in the melt are used.

The velocity in the melt is denoted by $\underline{v}(u, v, w)$, the pressure by p, and the temperature by T. The fluid density is denoted by ρ, the kinematic viscosity by ν, the thermal diffusivity by κ, and the surface tension by σ. The surface tension is taken to vary linearly with temperature $\sigma = \sigma_o - \gamma (T - T_m)$, where γ is the temperature coefficient and σ_o is the surface tension at the reference temperature, T_m.

The equations are non-dimensionalized using the half depth, L, the density at the reference temperature, ρ_o, an as yet undetermined velocity, U, and the temperature difference, ΔT. The pressure is non-dimensionalized using $\rho_o U \Omega L$. The resulting dimensionless governing equations for steady, axisymmetric flow in a frame of reference rotating with the zone are:

$$\epsilon\left(uu_r + wu_z - \frac{v^2}{r}\right) = -p_r + 2v + E\left(u_{rr} + \frac{u_r}{r} + u_{zz} - \frac{u}{r^2}\right) , \tag{1}$$

$$\epsilon\left(uv_r + wv_z + \frac{uv}{r}\right) = -2u + E\left(v_{rr} + \frac{v_r}{r} + v_{zz} - \frac{v}{r^2}\right) , \tag{2}$$

$$\epsilon(uw_r + ww_z) = -p_z + E\left(w_{rr} + \frac{w_r}{r} + w_{zz}\right) , \tag{3}$$

$$\Pr\epsilon(uT_r + wT_z) = E\left(T_{rr} + \frac{T_r}{r} + T_{zz}\right) , \tag{4}$$

$$u_r + \frac{u}{r} + w_z\ 0 , \tag{5}$$

where a suffix denotes differentiation with respect to that quantity. The dimensionless parameters, ϵ, E and Pr are defined below after equation (13).

The boundary conditions on the endwalls are for no flow and a constant temperature. On the sidewall, there is no radial flow and no azimuthal stress, and the axial temperature distribution leads to an axial thermocapillary stress. In dimensionless terms:

$$\left.\begin{array}{ll} u = v = w = 0 & \qquad (6a,b,c) \\ T = 0 . & \qquad (7) \end{array}\right\} \text{ on } z = \pm 1$$

$$\left.\begin{array}{ll} u = 0 , & \qquad (8) \\ v_r - \frac{v}{r} = 0 , & \qquad (9) \\ w_r = -MT_z , & \qquad (10) \\ T = \cos\frac{\pi z}{2} . & \qquad (11) \end{array}\right\} \text{ on } r = A$$

For an axisymmetric problem which is also symmetrical about mid-depth, the following must also be satisfied:

$$u = v = w_r = T_r = 0 , \quad \text{on } r = 0 , \tag{12}$$

$$u_z = v_z = w = T_z = 0 \quad , \quad \text{on } z = 0 \quad . \tag{13}$$

The dimensionless parameters are defined as follows: the aspect ratio $A = a/L$, the Ekman number $E = \nu/\Omega L^2$, the Rossby number $\epsilon = U/\Omega L$, the Prandtl number $Pr = \nu/\kappa$, the Marangoni number $M = \gamma \Delta T/\mu U$, where μ is the dynamic viscosity.

A stream function is introduced defined as,

$$w = -\frac{1}{r}(r\psi)_r \quad , \quad u = \psi_z \quad . \tag{14}$$

The global mass conservation condition is,

$$\psi = 0 \quad , \quad \text{on } r = A \text{ and } z = \pm 1 \quad . \tag{15}$$

2.2 Parameter Values

In order to make these theoretical studies as relevant as possible to real floating zone systems, silicon was chosen for the melt material and realistic values were chosen for the zone dimensions. Table 1 lists the values of the physical properties of silicon used in this paper. These values are the same as those used by Smith [7] and Smith and Greenspan [8] and they are taken from Reference 3. Table 2 lists the values of the zone dimensions and other quantities. The value of 5°C for ΔT may appear unrealistically small when the high melting point of silicon (1410°C) is considered but this is not necessarily so; this point is discussed further in Section VII. Table 3 lists the values of the dimensionless parameters. Since, at this stage in the paper U has not been determined, the values of ϵ and M cannot yet be calculated. However, for completeness the values calculated later (Section III) are included in Tables 2 and 3. The values of other dimensionless parameters to be discussed in Subsection 2.3 are also included in Table 3.

2.3 The Cylindrical Geometry Assumptions

The melt zone geometry is simplified to that of a right circular cylinder of fluid in uniform rotation (Fig. 2). The top and bottom endwalls were assumed to be plane. In a real floating zone system (Fig. 1), these boundaries are determined from a fuller set of equations and boundary conditions than are used here, and will, in general, be curved. However, the deviations from planarity can be made small in many cases.

In general, a liquid wets its solid phase and hence the contact angle (measured from the solid through the liquid to the face surface) is acute. This is true for silicon. To satisfy this boundary condition on plane parallel endwalls together with the interior zero-gravity condition of constant pressure, an hour-glass configuration, rather than a cylinder is required. However, since the melt extends out to the radius of the solid crystal rods, the contact angle will be formed on the curve at this edge and the surface at contact can be parallel to the symmetry axis. In this case, the solution for the free surface is a cylinder. With plane parallel endwalls in the presence of gravity (gravity parallel to the axis of symmetry), a quantitatively different hour-glass shape will form to satisfy the wetting boundary condition and the hydrostatic pressure gradient (Fig. 1).

TABLE 1. PHYSICAL PROPERTIES OF LIQUID SILICON AT 1410°C

Density	ρ_o	2.5 gm/cm^3
Dynamic Viscosity	μ	0.88 x 10^{-2} gm/cm sec
Kinematic Viscosity	ν	0.35 x 10^{-2} cm^2/sec
Thermal Conductivity	χ	0.32 Joule/cm sec C
Thermal Diffusivity	κ	0.15 cm^2/sec
Surface Tension	σ_o	720 dyne/cm
Temperature Coefficient of Surface Tension	γ	0.43 dyne/cm C

TABLE 2. DIMENSIONS OF THE FLOATING ZONE AND OTHER EXPERIMENTAL PARAMETERS

Depth	2L	2 cm
Radius	a	1 cm
Rotation Rate	Ω	1 rad/sec
Temperature Difference	ΔT	5 C°
Characteristic Flow Velocity	$U = \pi E^{1/3} \gamma \Delta T / 2\mu$	58 cm/sec

TABLE 3. DIMENSIONLESS PARAMETERS

Aspect Ratio, A	a/L	1
Ekman Number, E	$\nu/\Omega L^2$	0.35 x 10^{-2}
Prandtl Number, Pr	ν/κ	0.023
Marangoni Number, M	$\gamma \Delta T/\mu U$	4.2
Rossby Number, ε	$U/\Omega L$	58
Capillary Number, C	$\mu U/\sigma_o$	4.5 x 10^{-4}
Rotational Bond Number, B	$\rho_o \Omega^2 a^3/\sigma_o$	3.5 x 10^{-3}

Additional forces which can distort the cylindrical sidewall solution discussed above are the normal stresses due to viscosity and the centrifugal force. For the free surface to remain cylindrical, these stresses must be less than that due to surface tension. The ratios of the forces are measured by the capillary number $C = \mu U/\sigma_0$ and the rotational Bond number $B = \rho_0 \Omega^2 a^3/\sigma_0$, respectively, and for a flat cylindrical sidewall they should both be small. The values given in Tables 1 and 2 are used to derive, $C = 4.5 \times 10^{-4}$ and $B = 3.5 \times 10^{-3}$. Thus, for silicon and the dimensions chosen, a right circular cylinder of fluid is a good assumption.

III. ANALYTICAL SOLUTIONS

3.1 Linearization

Analytical solutions were found by linearizing equations (1) through (4). The momentum and temperature advection terms are dropped. This implies that the Rossby number, ϵ, is small.

3.2 The Temperature Solution

The temperature problem reduces to the solution of the two-dimensional conduction equation with the boundary conditions given by equations (7) and (11). The exact solution in nondimensional form is,

$$T = \frac{I_0(\pi r/2)}{I_0(\pi A/2)} \cos(\pi z/2) \quad , \tag{16}$$

where I_0 denotes the modified Bessel function of zero order. Since, as a consequence of the linearization, the temperature equation is decoupled from the flow field, equation (16) is the complete temperature solution for all of the analytical studies given in this paper.

3.3 The Interior Solution

For this paper's chosen conditions (Table 3), the Ekman number, E, is small and, hence, from equations (1) through (3) one expects viscous boundary layers on the zone boundaries and an interior flow in which viscous effects are small. The authors proceed using singular perturbation theory and expand to successive orders in E.

To leading order in E, equations (1), (2), (3), and (5) for the interior give:

$$-\frac{\partial p_I}{\partial r} + 2v_I = u_I = \frac{\partial p_I}{\partial z} = \frac{\partial w_I}{\partial z} = 0 \quad . \tag{17a,b,c,d}$$

Since there is no mechanism in this problem for establishing a radial pressure gradient, equations (17) reduce to:

$$u_I = v_I = w_I = p_I = \psi_I = 0 \quad . \qquad (18a,b,c,d,e)$$

Note that this interior solution satisfies all the endwall boundary conditions [equations (6)] and two sidewall boundary conditions [equations (8) and (9)], but it does not satisfy the thermocapillary stress condition [equation (10)].

3.4 The Leading Order $E^{1/3}$ Sidewall Boundary Layer

The flow conditions close to the sidewall are now examined. Smith [7] and Smith and Greenspan [8] in their study of the half zone found that a sidewall boundary layer of nondimensional thickness $E^{1/3}$ could satisfy the sidewall boundary conditions. For this problem an $E^{1/3}$ layer is also considered. To formulate the boundary layer equations and boundary conditions, a transformation to a dimensionless boundary layer coordinate, $\xi = E^{-1/3}\,(A-r)$, is made. The governing equations for this layer are well known [9] and are given in Appendix A. $w_{1/3} \sim 0(1)$ is defined, where the suffix, 1/3, denotes an $E^{1/3}$ layer quantity. The other amplitude scales are then found to be:

$$u_{1/3} \sim E^{1/3} \ , \ v_{1/3} \sim 0(1) \ , \ p_{1/3} \sim E^{1/3} \ , \ \psi_{1/3} \sim E^{1/3} \quad .$$

The $E^{1/3}$ layer has Ekman layers [9] associated with it on the endwalls. The Ekman compatibility condition [9] when transformed and scaled yields,

$$\tilde{w}_{1/3} = \pm \frac{1}{2} E^{1/6} \frac{\partial \tilde{v}_{1/3}}{\partial \xi} \quad , \quad \text{on} \quad z = \pm 1 \quad ,$$

where the tilda denotes an 0(1) quantity. To leading order, therefore, $\tilde{w}_{1/3}$ is zero. Thus, the axial flow in the $E^{1/3}$ layer recirculates and does not enter the Ekman layer. The boundary condition for the $E^{1/3}$ layer becomes $\tilde{w}_{1/3}$ or $\tilde{\psi}_{1/3} = 0$, on $z = \pm 1$.

The axial thermocapillary stress boundary condition, equation (10), when transformed to the boundary layer coordinate and scaled becomes

$$\frac{\partial \tilde{w}_{1/3}}{\partial \xi} = -\frac{1}{2} E^{1/3} M\pi \sin \frac{1}{2}\pi z \quad = \frac{E^{1/3}\,\pi\gamma\Delta T}{2\mu U} \sin \frac{1}{2}\pi z \quad .$$

Since the boundary layer thickness has now been determined, the characteristic velocity, U, can be determined by balancing viscous shear against the thermocapillary stress. The equation

$$U = \frac{E^{1/3}\,\pi\gamma\Delta T}{2\mu}$$

is obtained and the thermocapillary stress boundary condition reduces to

$$\frac{\partial w_{1/3}}{\partial \xi} + \sin\left(\frac{1}{2}\pi z\right) = 0 \quad \text{on } \xi = 0 \ .$$

The azimuthal stress boundary condition, equation (9), when transformed and scaled becomes,

$$\frac{\partial v_{1/3}}{\partial \xi} = 0 \quad \text{on } \xi = 0 \ .$$

When solving for the $E^{1/3}$ layer, the problem is formulated in terms of $\tilde{\psi}_{1/3}$, and

$$\frac{\partial^5 \tilde{\psi}_{1/3}}{\partial \xi^5} = 0 \quad \text{on } \xi = 0$$

is used for the azimuthal stress condition. This condition is equivalent to

$$\frac{\partial}{\partial z} \frac{\partial \tilde{v}_{1/3}}{\partial \xi} = 0 \quad \text{on } \xi = 0 \ .$$

Thus, the authors actually solved for a constant stress. However, this constant turns out to be zero for this solution. The boundary conditions and solutions for the $E^{1/3}$ layer are given in Appendix A.

Now that a characteristic velocity, U, has been determined, the values for ϵ and M can be calculated and are given in Table 3. It is noted that ϵ is not small. Since, for the linear results to be valid, ϵ must be small, the question of the value of the linear work is raised. For the linear floating zone problem being studied, analytical solutions can be found and this means that there is a complete description of the flow dynamics. In general, analytical solutions cannot be found for strongly nonlinear problems. The great value of linear results is that they provide a frame of reference for analyzing the nonlinear contributions. Nonlinear effects can often be seen as secondary influences on the basic linear flow even for relatively large values of the parameter estimating the nonlinearity. The linear results were found to be valuable for interpreting the weakly and strongly nonlinear results presented in this paper. Also, the results presented in this paper reveal that ϵ may not be so large for a more realistic model, thus reducing the nonlinear effects.

3.5 The Ekman Layers Associated with the $E^{1/3}$ Layer

The $E^{1/3}$ layer azimuthal flow, $\tilde{v}_{1/3}$ [equation (A-13)], does not vanish on the endwalls. Ekman layers are required on these boundaries to satisfy the no-slip condition. This report now proceeds to examine these layers. A transformation to $\zeta = E^{-1/2}(1-z)$ is made. This discussion is limited to the Ekman layer at $\zeta = 1$. [A similar discussion for the Ekman layer at z = –1 is pursued using the transformation, $\zeta' = E^{-1/2}(1 + z)$.] Taking $v_{1/2} \sim 0(1)$ to match $v_{1/3}$ and satisfy the no-slip condition on the endwall, the following amplitude scales are obtained for the Ekman layer:

$$u_{1/2} \sim 0(1) \ , \ w_{1/2} \sim E^{1/6} \ , \ p_{1/2} \sim E^{2/3} \ , \ \psi_{1/2} \sim E^{1/2} \ .$$

Since $u_{1/2} > u_{1/3}$ the appropriate boundary condition is that $u_{1/2} = 0$ on $\zeta = 0$. The equations, boundary conditions, and solutions for this layer are given in Appendix B.

3.6 The First Order $E^{1/3}$ Sidewall Boundary Layer and the $E^{1/4}$ Sidewall Boundary Layer

This section now proceeds systematically to improve the accuracy of the results. The largest neglected term is in the boundary condition, $w = 0$, on the endwalls. One has $w_{1/3} = 0$, but $w_{1/2} \sim E^{1/6}$. Therefore, a first order $E^{1/3}$ sidewall boundary layer, with all the previous scales multiplied by the factor $E^{1/6}$, is introduced. These amplitude scales are:

$${}_1u_{1/3} \sim E^{1/2} \ , \ {}_1v_{1/3} \sim E^{1/6} \ , \ {}_1w_{1/3} \sim E^{1/6} \ , \ {}_1p_{1/3} \sim E^{1/2} \ , \ {}_1\psi_{1/3} \sim E^{1/2} \ .$$

The preceding suffix 1 denotes a first order quantity. The equations are given in Appendix C.

Ekman compatibility yields,

$${}_1\tilde{\psi}_{1/3} = \pm \frac{1}{2} \tilde{v}_{1/3} \quad , \quad \text{on} \ \ z = \pm 1 \quad . \tag{19}$$

To proceed there is no need to solve for the first order $E^{1/3}$ layer, but the azimuthal stress boundary condition must be examined. Since the leading order $E^{1/3}$ layer satisfies the vanishing azimuthal stress condition, an attempt is made to apply the same condition to the first order layer. Consider the following integrated form of equation (C-7),

$$\int_{-1}^{+1} \int_{0}^{\infty} \frac{\partial^2 \ {}_1\tilde{v}_{1/3}}{\partial \xi^2} \, d\xi \, dz = 2 \int_{-1}^{+1} \int_{0}^{\infty} \frac{\partial_1 \tilde{\psi}_{1/3}}{\partial z} \, d\xi \, dz \quad ,$$

i.e.

$$- \int_{-1}^{+1} \frac{\partial_1 \tilde{v}_{1/3}}{\partial \xi} \bigg|_{\xi=0} dz = 2 \int_{0}^{\alpha} \left({}_1\tilde{\psi}_{1/3} \big|_{z=1} - {}_1\tilde{\psi}_{1/3} \big|_{z=-1} \right) d\xi \quad .$$

Using equation (19), one obtains,

$$\int_{-1}^{+1} \frac{\partial_1 \tilde{v}_{1/3}}{\partial \xi} \bigg|_{\xi=0} dz = -2 \int_{0}^{0} \tilde{v}_{1/3} \big|_{z=1} \, d\xi \quad . \tag{20}$$

The left-hand side of equation (20) is the integrated azimuthal sidewall stress and the right-hand side is not zero, hence, the first order $E^{1/3}$ layer cannot satisfy a vanishing azimuthal stress condition. A further boundary layer is required.

Sidewall layers of thickness $E^{1/4}$ are well known in the rotating fluids literature and are usually invoked to satisfy azimuthal flow boundary conditions [9]. An $E^{1/4}$ layer is introduced to satisfy the azimuthal stress requirement. It is known from the previous work on $E^{1/4}$ layers that the sidewall azimuthal stress is constant [see also equation (D-11)], independent of z. Thus, the first order $E^{1/3}$ layer azimuthal stress is taken to be independent of z, i.e.,

$$\frac{\partial}{\partial z}\left(\frac{\partial\, {}_1\tilde{v}_{1/3}}{\partial \xi}\right) = 0 \quad , \quad \text{on } \zeta = 0 \quad , \tag{21}$$

which can be written as

$$\frac{\partial^5\, {}_1\tilde{\psi}_{1/3}}{\partial \xi^5} = 0 \quad , \quad \text{on } \xi = 0 \quad .$$

This discussion on the formulation of the first order $E^{1/3}$ layer problem is completed by remembering that the leading order sidewall layer satisfies the no radial flow boundary condition and the axial thermocapillary stress condition, therefore,

$${}_1\tilde{\psi}_{1/3} = \frac{\partial^2\, {}_1\tilde{\psi}_{1/3}}{\partial \xi^2} = 0 \quad , \quad \text{on } \xi = 0 \quad ,$$

is required. The complete set of boundary conditions is given in Appendix C.

To formulate the $E^{1/4}$ sidewall layer equations and boundary conditions, one transforms to a boundary layer coordinate, η, using $\eta = E^{-1/4}(A-r)$. The amplitude scales of the $E^{1/4}$ layer are determined by equating the magnitudes of the first order $E^{1/3}$ layer and $E^{1/4}$ layer azimuthal stresses. One obtains

$$u_{1/4} \sim E^{7/12} \quad , \quad v_{1/4} \sim E^{1/12} \quad , \quad w_{1/4} \sim E^{1/3} \quad , \quad p_{1/4} \sim E^{1/3} \quad , \quad \psi_{1/4} \sim E^{7/12} \quad .$$

This report now proceeds to find the expression for the first order $E^{1/3}$ layer azimuthal stress and hence for the $E^{1/4}$ layer azimuthal stress. The required boundary condition is,

$$\frac{\partial\, {}_1\tilde{v}_{1/3}}{\partial \xi} + \frac{\partial \tilde{v}_{1/4}}{\partial \eta} = 0 \quad , \quad \text{on } \xi = \eta = 0 \quad . \tag{22}$$

From equation (A-12) one obtains,

$$\int_0^\infty \tilde{v}_{1/3}\Big|_{z=1} d\xi = \sum_{n=1}^\infty (-1)^{n+1} \frac{a_n}{\gamma_n^2} \quad . \tag{23}$$

Substituting equation (23) into equation (20) one obtains,

$$\int_{-1}^{+1} \frac{\partial_1 \tilde{v}_{1/3}}{\partial \xi}\Big|_{\xi=0} dz = -2\sum_{n=1}^\infty (-1)^{n+1} \frac{a_n}{\gamma_n^2} \quad . \tag{24}$$

Using equation (21), equation (24) can be integrated to give,

$$\frac{\partial_1 \tilde{v}_{1/3}}{\partial \xi}\Big|_{\xi=0} = -\sum_{n=1}^\infty (-1)^{n+1} \frac{a_n}{\gamma_n^2} \quad . \tag{25}$$

Finally, from equations (22) and (25) one obtains,

$$\frac{\partial \tilde{v}_{1/4}}{\partial \eta}\Big|_{\eta=0} = \sum_{n=1}^\infty (-1)^{n+1} \frac{a_n}{\gamma_n^2} \quad . \tag{26}$$

Note that the $E^{1/4}$ azimuthal stress boundary condition has been found without solving for the first order $E^{1/3}$ layer.

The equations, boundary conditions, and solutions for the $E^{1/4}$ layer are given in Appendix D. The boundary conditions and solutions for the Ekman layer associated with the $E^{1/4}$ layer are also given in Appendix D.

An attempt was made to solve for the first order $E^{1/3}$ sidewall layer and solutions involving multiple summation were obtained. The convergence properties of these forms presented substantial difficulties to the numerical computation of the solutions. Also, since accurate solutions for the linear problem were obtained using numerical methods (see Section 4) and since the essential dynamics of the linear flow are revealed without finding complete solutions (see Section 6), no analytical solutions for the first order $E^{1/3}$ sidewall layer are given.

3.7 The Composite Analytical Solutions

The dimensional analytical results for the leading order $E^{1/3}$ layer and its associated Ekman layer with the addition of the $E^{1/4}$ layer and its associated Ekman layer are shown in Figures 3. Figures 3 include the stream function, azimuthal velocity, temperature, axial velocity, radial velocity, and pressure. It should be noted that these plots do not include the first order $E^{1/3}$ layer. These results are discussed further in Sections 5 and 6.

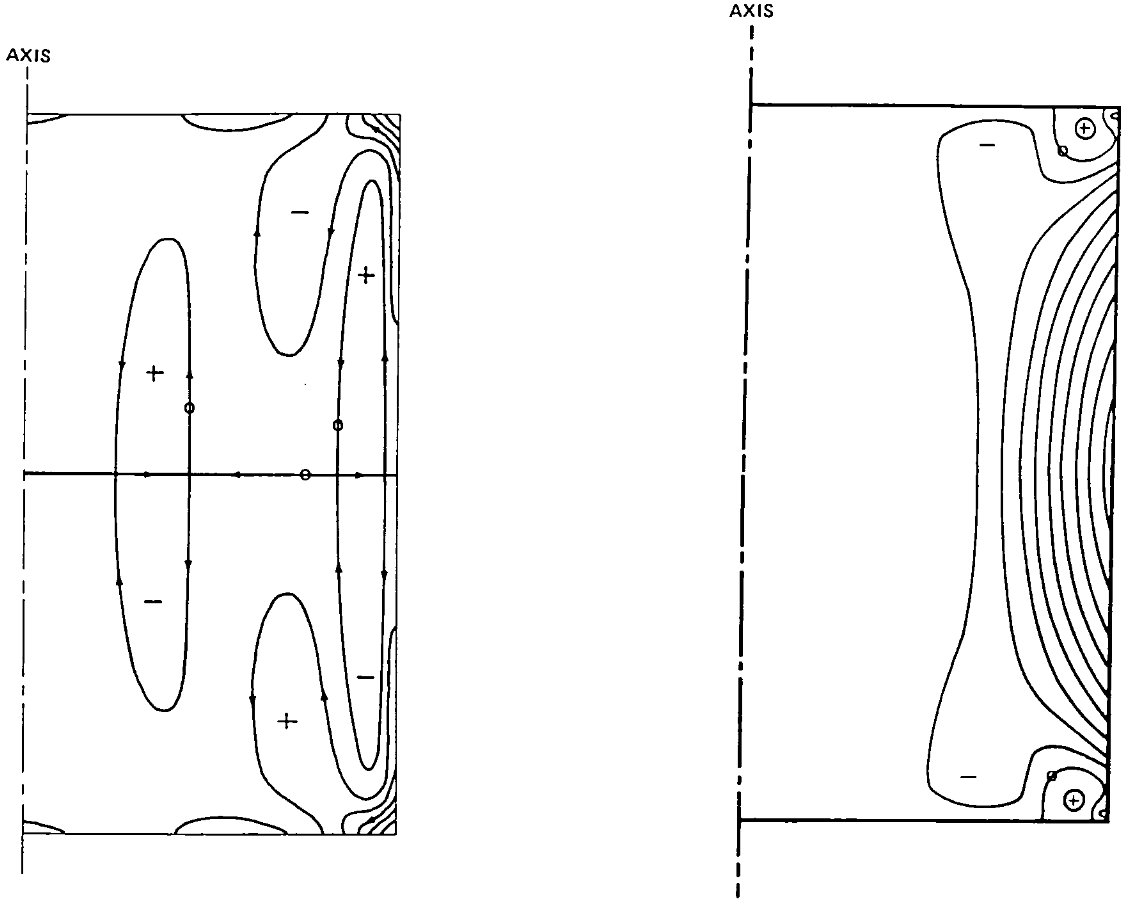

(a) Stream Function (cm^2/sec); 1.10 x 10^{-4}; -1.10 x 10^{-4}; 2 x 10^{-5}.

(b) Azimuthal velocity (cm/sec); 3.51 x 10^{-4}; -2.76 x 10^{-3}; 3 x 10^{-4}.

Figure 3. The dimensional analytical solutions for the dependent quantities. Each solution consists of the sum of the leading order $E^{1/3}$ layer and its associated Ekman layer and the $E^{1/4}$ layer and its associated Ekman Layer. The first order $E^{1/3}$ layer is not included. To facilitate comparison with the linearized numerical results (Figs. 4), the analytical results are calculated for the same parameter values ($\Delta T = 5 \times 10^{-4}$°C, $A = 1$, $E = 0.35 \times 10^{-2}$, $Pr = 0.023$). The dependent variables are listed below each figure together with the dimensional maximum and minimum values and the contour increment. For the pressure, only the contour increment is given.

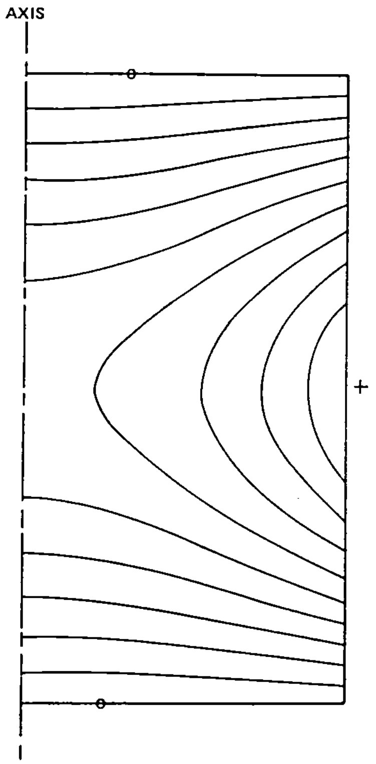

(c) Temperature (°C); 5 x 10^{-4}; 0; 0.5 x 10^{-4}.

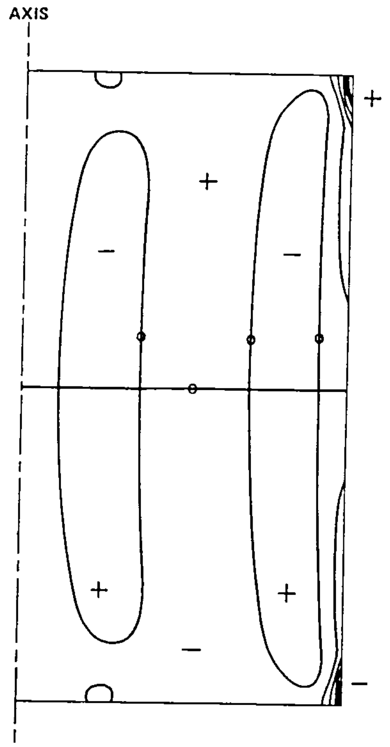

(d) Axial Velocity (cm/sec); 5.64 x 10^{-3}; -5.64 x 10^{-3}; 8 x 10^{-4}.

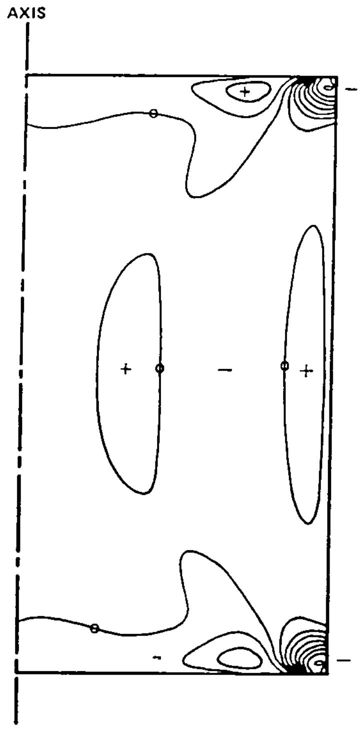

(e) Radial Velocity (cm/sec); 2.52 x 10^{-4}; -1.38 x 10^{-3}; 1 x 10^{-4}.

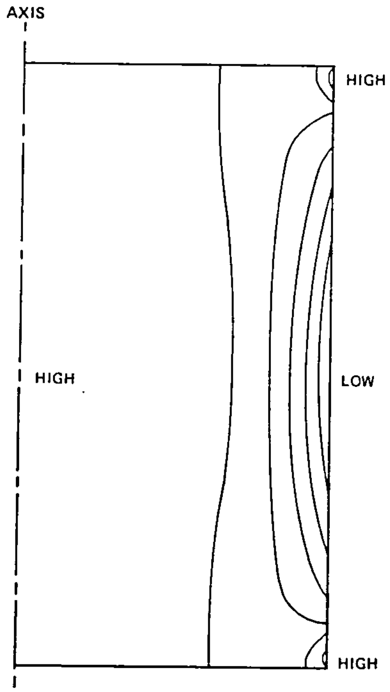

(f) Pressure (cm^2/sec^2); 2 x 10^{-4}.

IV. NUMERICAL SOLUTIONS

4.1 The Numerical Model

In Section III it was found that the dimensionless parameter, ϵ, multiplying the nonlinear terms in the governing equations, is not small for the parameters and model chosen. Thus, the linearized results, although valuable for understanding the flows and the flow confinement dynamics (see Subsection 3.4), cannot be considered as accurate. A numerical model was used to include nonlinear effects in these studies.

For this work a code already developed for the Atmosphere General Circulation Experiment (AGCE) Program [11] was modified. The code is discussed in some detail by Fowlis and Roberts [12] and additional applications of the code, including the floating zone application, are described by Roberts et al. [13]. The numerical methods used in the code are described briefly in Appendix E. The original AGCE code was developed for a spherical shell configuration with inner and outer spherical boundaries and radial, latitudinal boundaries. The conversion to cylindrical geometry was carried out by making the radius of the inner sphere very large and considering only the small latitudinal range from the axis of symmetry to the outer latitudinal boundary which becomes the floating zone sidewall. The boundary conditions on the sidewall were modified to allow for a free surface in the presence of the axial thermocapillary stress.

The code was thoroughly validated in its cylindrical form using accurate and detailed experimental measurements obtained using laser-Doppler velocimetry. The validations studied used the experimental data presented by Warn-Varnas et al. [14] and Hyun et al. [15,16] and excellent agreement was obtained for both linear and nonlinear flows.

4.2 Numerical Results

All the numerical results presented in this subsection were examined to be certain that the spatial resolution was satisfactory and that convergence occurred. Initially, a nonuniform grid of 25 (radial mesh points) x 40 (axial mesh points) was used, but, if the results indicated that more resolution was required, the grid resolution was systematically increased. The maximum number of grid points used was 40 x 120 and with this resolution even the strongly nonlinear, unsteady flow was resolved. The iterative method for rapid convergence to a steady-state was used (see Appendix E). However, to be certain that a steady-state was the correct solution, the results were confirmed using uniform time-stepping. The unsteady flows were determined using time-stepping. As a consequence of the above and the validation studies described in Subsection 4.1, the numerical solutions presented are considered to be accurate solutions of the governing two-dimensional equations [equations (1) to (5)]. However, for nonlinear systems the solution computed is not necessarily unique. Different initial conditions can lead to different solutions (hysteresis effects). Further, as the nonlinearity is increased the flow is more likely to become unstable to azimuthal perturbations.

To check the analytical results, an effectively linear flow was first computed. This was done by reducing ΔT from 5°C to 5×10^{-4}°C, thus reducing ϵ to 5.8×10^{-3}, and keeping the same values for the other dimensionless parameters (see Table 3). The dimensional results for stream function, azimuthal velocity, temperature, axial velocity, radial velocity, and pressure are shown in Figures 4. A nonuniform grid of 25 x 40 and the iterative method for convergence were used. The linear flow results are discussed further in Sections V and VI.

To examine the effects of nonlinearity, the code for $\Delta T = 0.5$°C, corresponding to $\epsilon = 5.8$, was run, again keeping the same values for the other dimensionless parameters (see Table 3). The dimensional results

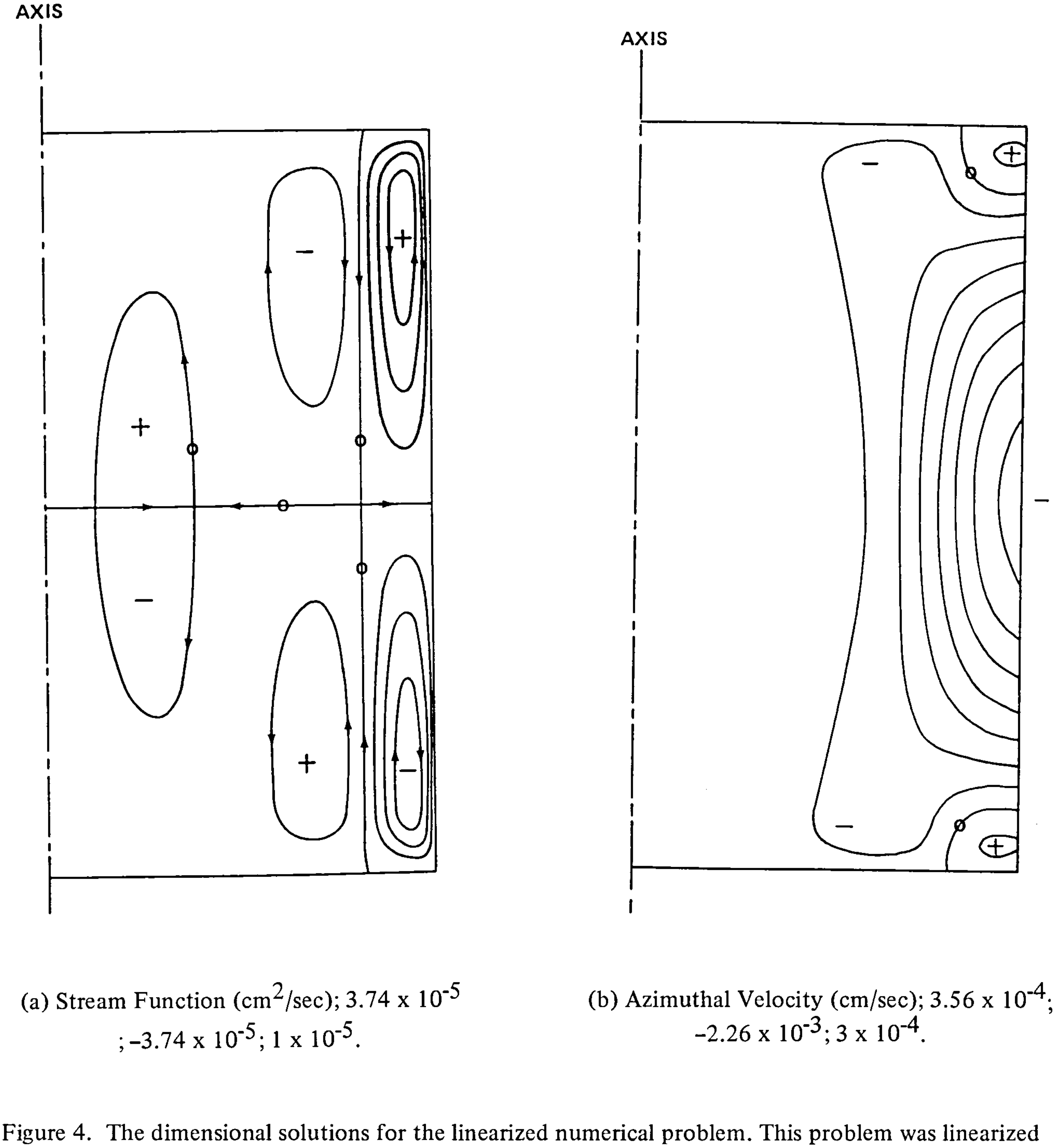

(a) Stream Function (cm^2/sec); 3.74 x 10^{-5} ; -3.74 x 10^{-5}; 1 x 10^{-5}.

(b) Azimuthal Velocity (cm/sec); 3.56 x 10^{-4}; -2.26 x 10^{-3}; 3 x 10^{-4}.

Figure 4. The dimensional solutions for the linearized numerical problem. This problem was linearized by taking $\Delta T = 5 \times 10^{-4}$°C and hence, $\epsilon = 0.58 \times 10^{-2}$. The other parameters have the values, $A = 1$, $E = 0.35 \times 10^{-2}$, $Pr = 0.023$. The dependent variables are listed below each figure together with the dimensional maximum and minimum values and the contour increment. For the pressure, only the contour increment is given.

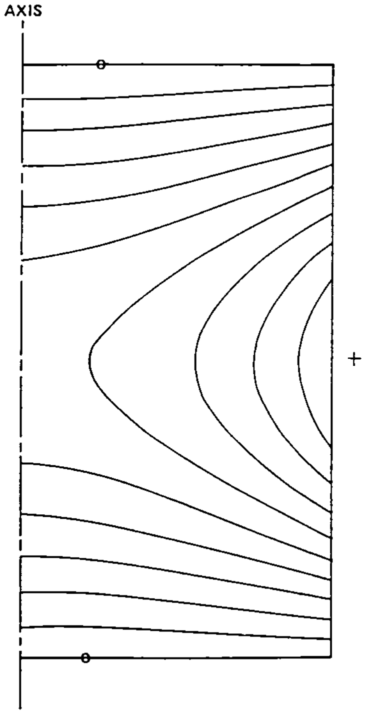

(c) Temperature (°C); 5 x 10^{-4}; 0; 5 x 10^{-5}.

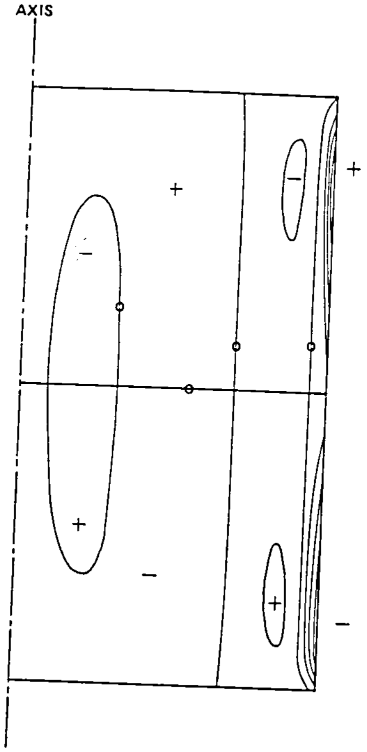

(d) Axial Velocity (cm/sec); 1.48 x 10^{-3}; -1.48 x 10^{-3}; 4 x 10^{-4}.

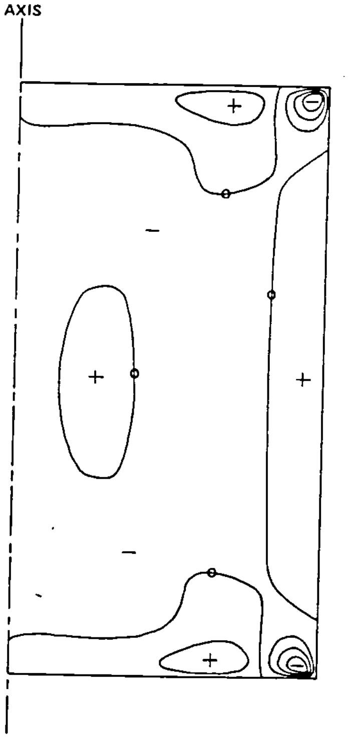

(e) Radial Velocity (cm/sec); 1.88 x 10^{-4}; -3.96 x 10^{-4}; 1 x 10^{-4}.

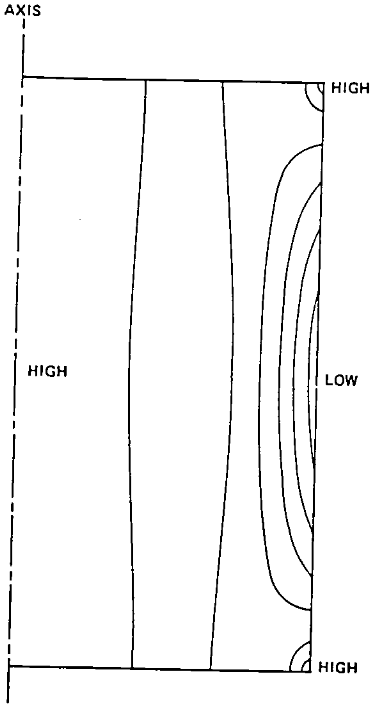

(f) Pressure (cm^2/sec^2); 2 x 10^{-4}.

for stream function, azimuthal velocity, temperature, axial velocity, radial velocity, and pressure are shown in Figures 5. The results presented were computed with a nonuniform grid of 40 x 120 and time-stepping for about 60 sec from an initial state of no motion relative to the rotating frame of reference. However, the iterative method gave identical results. Note that the flow patterns are significantly different from the linearized results of Figures 4. These results are discussed further in Section 6.

Finally, the code for $\Delta T = 5°C$, corresponding to $\epsilon = 58$, was run, keeping the same values for the other parameters (see Table 3). This strongly nonlinear flow did not achieve a steady-state but settled to a flow with a weak oscillation. The dimensional results for two extreme phases of the oscillation are shown in Figures 6 and 7; stream function, azimuthal flow, and temperature plots are presented. These results were computed with a nonuniform grid of 40 x 120 and time-stepping for about 40 sec from an initial state of no relative motion. This flow was also examined starting from the same initial state but using the iterative method for a time estimated as 20 sec and then time-stepping for another 25 sec. The solutions achieved were essentially the same as those presented in Figures 6 and 7. These results are discussed further in Section VI.

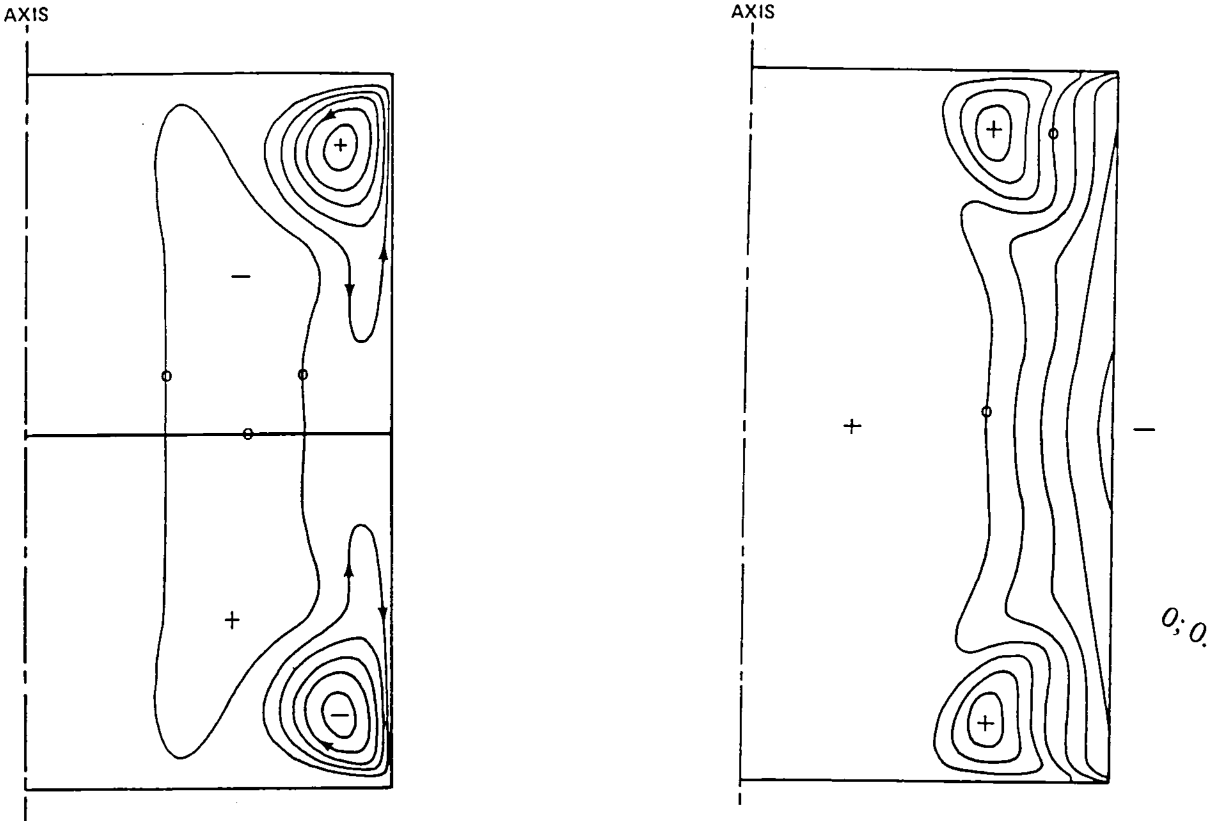

(a) Stream Function (cm^2/sec); 8.10 x 10^{-2}; -8.10 x 10^{-2}; 1.5 x 10^{-2}.

(b) Azimuthal Velocity (cm/sec); 0.351; -0.417; 0.1.

Figure 5. The dimensional solutions for the weakly nonlinear flow. For this problem $\Delta T = 0.5°C$ and hence, $\epsilon = 5.8$. The other parameters have the values, $A = 1$, $E = 0.35 \times 10^{-2}$, $Pr = 0.023$. The dependent variables are listed below each figure together with the dimensional maximum and minimum values and the contour increment. For the pressure, only the contour increment is given.

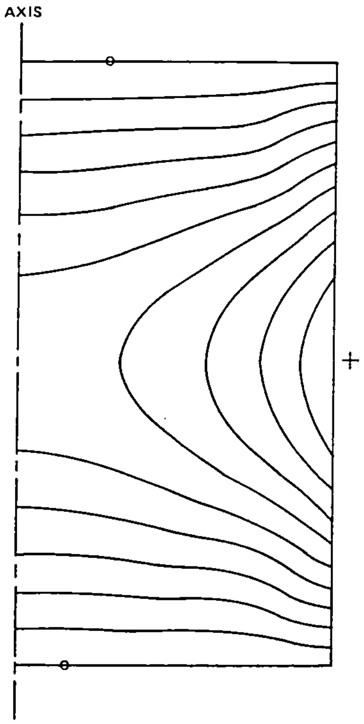

(c) Temperature (°C); 0.5; 0; 5 x 10^{-2}.

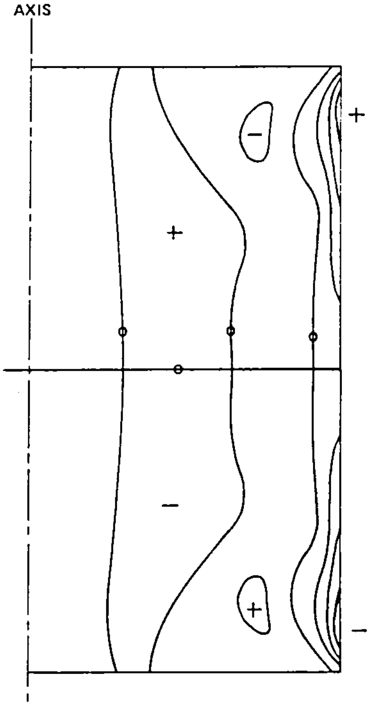

(d) Axial Velocity (cm/sec); 1.79; −1.74; 0.5.

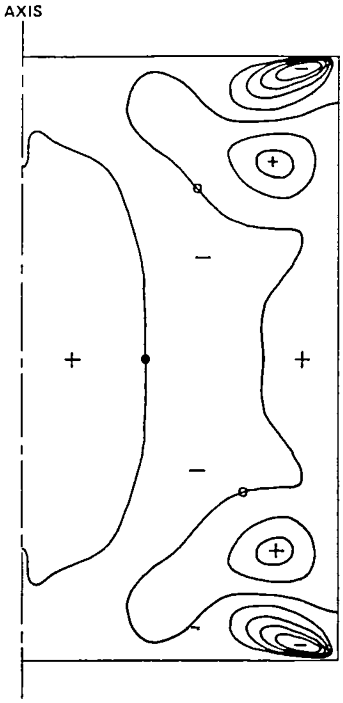

(e) Radial Velocity (cm/sec); 0.458; −1.01; 0.2.

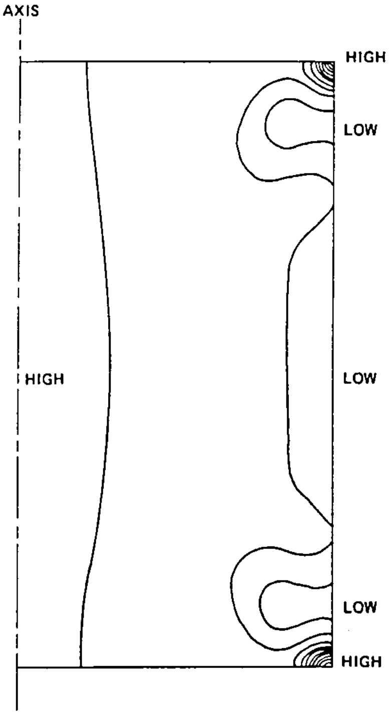

(f) Pressure (cm^2/sec^2); 0.2.

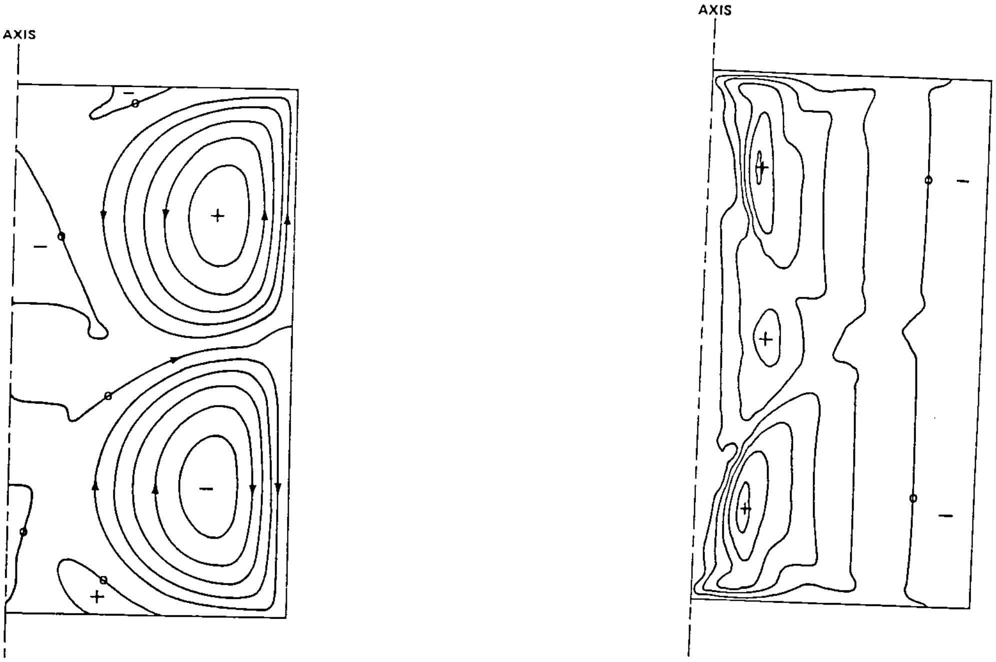

(a) Stream Function (cm^2/sec); 0.846; -0.840; 0.15. (b) Azimuthal Velocity (cm/sec); 2.65; -0.432; 0.5.

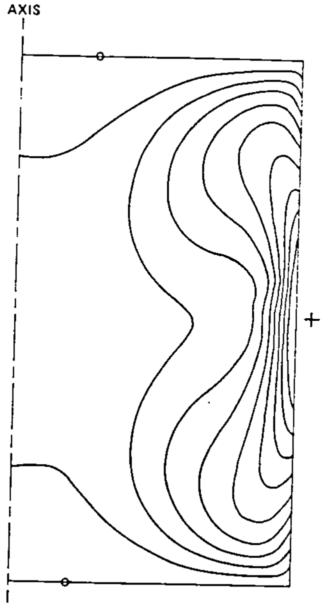

(c) Temperature (°C); 5.00; 0; 0.5.

Figure 6. The dimensional solutions for the strongly nonlinear flow. For this problem $\Delta T = 5°C$ and hence, $\epsilon = 58$. The other parameters have the values, $A = 1$, $E = 0.35 \times 10^{-2}$, $Pr = 0.023$. This figure shows an extreme phase of the observed oscillation; Figure 7 shows the other extreme phase. The dependent variables are listed below each figure together with the dimensional maximum and minimum values and the contour increment.

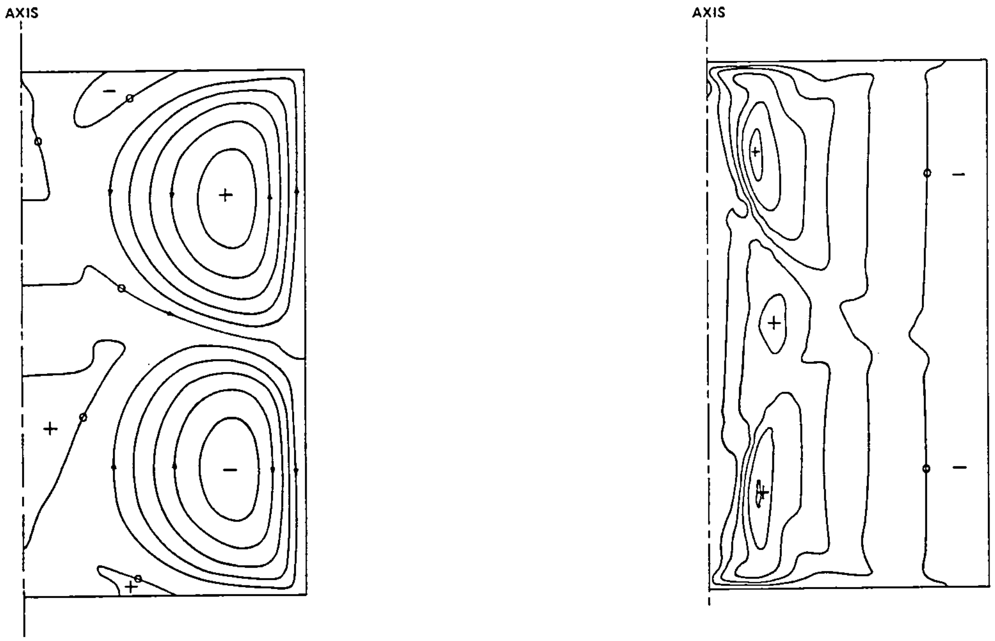

(a) Stream Function (cm^2/sec); 0.840; -0.847; 0.15. (b) Azimuthal Velocity (cm/sec); 2.66; -0.435; 0.5.

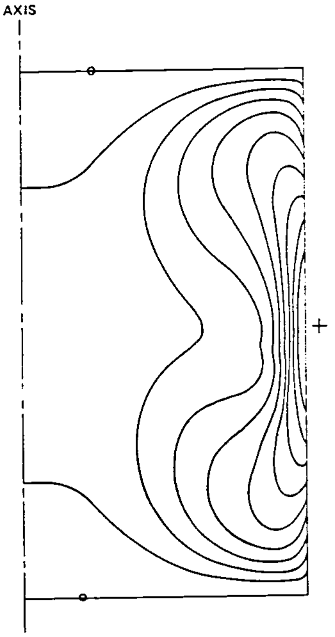

(c) Temperature (°C); 5.00; 0; 0.5.

Figure 7. The dimensional solutions for the strongly nonlinear flow. For this problem $\Delta T = 5°C$ and hence, $\epsilon = 58$. The other parameters have the values, $A = 1$, $E = 0.35 \times 10^{-2}$, $Pr = 0.023$. This figure shows an extreme phase of the observed oscillation; Figure 6 shows the other extreme phase. The dependent variables are listed below each figure together with the dimensional maximum and minimum values and the contour increment.

V. COMPARISON OF THE ANALYTICAL AND LINEARIZED NUMERICAL RESULTS

The analytical results (Fig. 3) are now compared with the linearized numerical results (Fig. 4). It should be remembered that Figures 3 do not include the first order $E^{1/3}$ layer and that some higher order flows do not satisfy the boundary conditions.

Very good agreement between the analytical and numerical results is obtained for the azimuthal flow in both overall contour shapes and maximum and minimum values (see Figs. 3b and 4b). For the analytical results the azimuthal stress due to the $E^{1/3}$ layer vanishes on the sidewall. The combined azimuthal stress due to the first order $E^{1/3}$ layer and the $E^{1/4}$ layer also vanishes on the sidewall but, of course, the first order $E^{1/3}$ layer is not included in Figure 4b. The amplitude of $v_{1/3}$ is $0(1)$ and the omitted $v_{1/3} \sim E^{1/6}$ (0.39) is less than $v_{1/4} \sim E^{1/12}$ (0.62).

The numbers in parentheses after the amplitude scales show the magnitudes of the amplitude scales for the particular variables. These values are based on $E = 0.35 \times 10^{-2}$ (see Table 3). Since E is not exceedingly small, the amplitudes just discussed, and those in the discussion to follow, are sometimes not very different. Thus, these amplitude comparisons should not be taken as truly quantitative, since factors in the exact solutions could make significant contributions.

Good agreement is obtained for the axial flow in both overall contour shape and maximum and minimum values (see Figs. 3d and 4d). For the analytical results, the $E^{1/3}$ layer satisfies the axial thermocapillary stress. However, the axial stress due to the $E^{1/4}$ layer does not vanish on the sidewall. The amplitude of $w_{1/3}$ is $0(1)$ but the omitted ${}_1w_{1/3} \sim E^{1/6}$ (0.39) is not less than $w_{1/4} \sim E^{1/3}$ (0.15).

Good agreement is obtained for the radial flow in overall contour shape but there is not good agreement for flow magnitudes (see Figs. 3e and 4e). Note that the extreme negative values for the radial flow occur in the sidewall corner regions and that these regions are not resolved in the analytical work. For the analytical results the radial flow due to the $E^{1/3}$ layer vanishes on the sidewall [see equation (A-13)] but the radial flow due to the $E^{1/3}$ layer, Ekman layer does not vanish on the sidewall [see Fig. 4e and equation (B-10)]. Also, the radial flow due to the $E^{1/4}$ layer does not vanish on the sidewall [see Fig. 4d and equation (D-10)]. The amplitude of $u_{1/3}$ is $0(E^{1/3})$ (0.15) but the omitted ${}_1u_{1/3} \sim E^{1/2}$ (0.059) is not less than $u_{1/4} \sim E^{7/12}$ (0.037). Good agreement is obtained for the pressure (see Figs. 3f and 4f). The amplitude of $p_{1/3}$ is $0(E^{1/3})$ (0.15) and the omitted ${}_1p_{1/3} \sim E^{1/2}$ (0.059) is less than $p_{1/4} \sim E^{1/3}$ (0.15). Poor agreement is obtained for the stream function (see Figs. 3a and 4a). For the analytical results this is a consequence of the radial flow at the sidewall due to the $E^{1/4}$ layer. The amplitude of $\psi_{1/3}$ is $0(E^{1/3})$ (0.15) but the omitted $\psi_{1/3} \sim E^{1/4}$ (0.059) is not less than $\psi_{1/4} \sim E^{7/12}$ (0.037). To reduce the $E^{1/4}$ layer radial flow at the sidewall to zero, it is necessary to introduce a second order $E^{1/3}$ layer. The analytical studies were not pursued beyond this point. As expected, the temperature results are identical (see Figs. 3c and 4c).

VI. DISCUSSION OF RESULTS

6.1 The Linear Flow

The agreement between the analytical and linearized numerical results and the authors understanding of the discrepancies between these results (see Section V) are such that it is believed the analytical results reveal the essential dynamics of the linear flow. Since the linear flow is symmetrical about the mid-depth plane of the floating zone, the following discussion is confined to one half of the full floating zone. The surface tension of liquid silicon increases with decreasing temperature, hence, the sidewall stress pulls fluid away from the mid-depth plane towards the endwalls. In the vicinity of the endwall most of this fluid turns around before entering the Ekman layer and circulates in an $E^{1/3}$ sidewall layer. As a consequence of the basic rotation, the inward radial flow near the endwall leads to positive azimuthal flow and the outward radial flow near the mid-depth plane leads to negative azimuthal flow. The azimuthal flow near the endwall drives an Ekman layer on that wall over the $E^{1/3}$ layer. The Ekman layer has a meridional flow which circulates through a first order $E^{1/3}$ layer. The flow from the first order layer enters the Ekman layer in the corner region, not resolved by the analytical studies, then returns directly from the Ekman layer.

The leading order $E^{1/3}$ layer satisfies all the sidewall boundary conditions, but the first order layer cannot satisfy the sidewall azimuthal stress condition. Thus, an $E^{1/4}$ layer with negative azimuthal flow exists in which the meridional flow circulates in the opposite sense. In combination with the first order $E^{1/3}$ layer, this $E^{1/4}$ layer satisfies the vanishing azimuthal stress condition. The high order radial flow and the axial stress introduced by the $E^{1/4}$ layer remain unsatisfied and require the presence of a still higher order $E^{1/3}$ layer (or layers).

In agreement with what was found by Smith [7] and Smith and Greenspan [8], these linearized results (see Fig. 4) show, for the weak thermocapillary flow, that rotation does confine the flow to sidewall boundary layers and that there is no flow in the interior of the melt relative to the rotating endwalls. For comparison, the flow for identical conditions to the flow of Figures 4, except that the rotation rate was made zero, is shown in Figures 8. Figures 8 show the stream function, the axial velocity, and the radial velocity. The azimuthal flow is not shown since it is zero for a nonrotating flow and the temperature is not shown since it is virtually identical to the conduction solution (see Fig. 4c). [The nonrotating results were computed for a nonuniform 40 x 70 mesh and the iterative method (see Appendix E) was used.] It is seen that this flow is considerably stronger than the rotating flow and that it penetrates much more deeply into the interior of the melt.

For the half zone, Smith [7] and Smith and Greenspan [8] did not require an $E^{1/4}$ layer. Thus, the presence of this thicker layer in the full zone means that confinement is not quite as good as for the half zone. The boundary layers could be made thinner by increasing the rotation rate, Ω, and hence decreasing E.

Increasing Ω will also increase the flow due to centrifugal buoyancy and it should be remembered that this flow has been neglected in the present study. Smith [7] and Smith and Greenspan [8] studied the linearized flow due to centrifugal buoyancy in the half zone. They found a flow which circulated through the interior via Ekman layers on the endwalls. But, for the conditions given in Tables 1 and 2, they found this flow to be much weaker than the thermocapillary flow. For the full zone this flow will be still weaker, since in this configuration one cannot have Ekman layers at the mid-depth plane allowing for radial

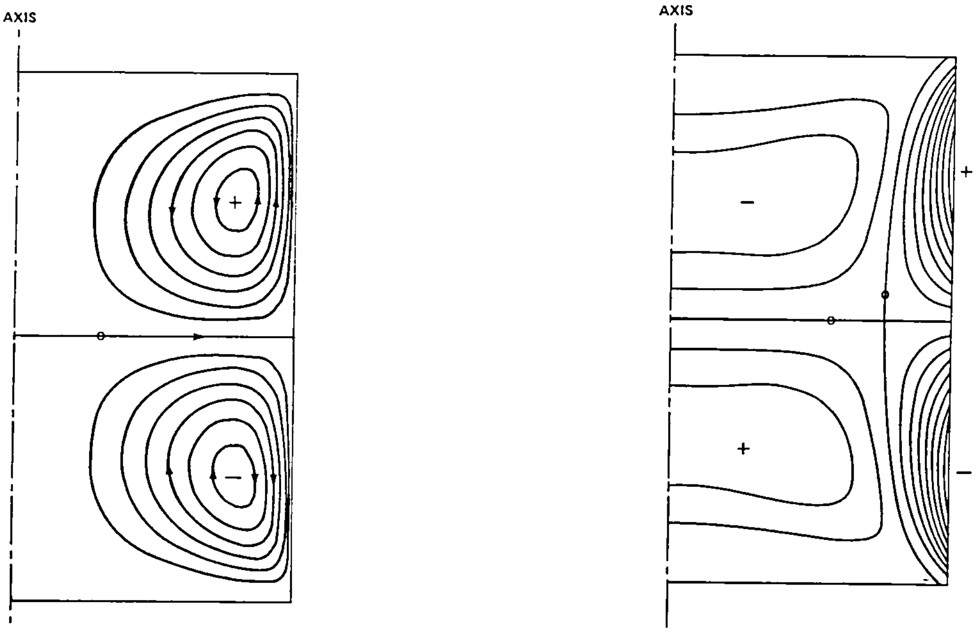

(a) Stream Function (cm^2/sec); 3.24×10^{-4}; -3.24×10^{-4}; 5×10^{-5}.

(b) Axial Velocity (cm/sec); 4.04×10^{-3}; -4.04×10^{-3}; 5×10^{-4}.

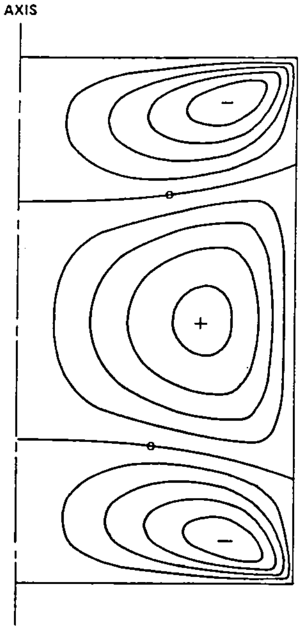

(c) Radial Velocity (cm/sec); 1.29×10^{-3}; -1.43×10^{-3}; 3×10^{-4}.

Figure 8. The dimensional solutions for the nonrotating flow and for $\Delta T = 5 \times 10^{-4}$°C. The other parameters have the values, $A = 1$, $Pr = 0.023$. The dependent variables are listed below each figure together with the dimensional maximum and minimum values and the contour increment.

fluid motion. Another parameter to be considered as Ω is increased in the rotational Bond number, B (see Section II). For the cylindrical geometry of this model to remain accurate B must remain small.

For this work realistic values were chosen for a floating zone system. As a consequence, although E is small, it is not very small and the ratios between the amplitudes of the higher order and lower order boundary layer quantities are not particularly small, It could be argued that to check further this analytical theory, one should perform numerical studies for smaller values of E and look for systematic converge of the analytical and numerical results. Some such studies were performed and convergence was observed. However, since the linearized flow is somewhat unrealistic and was performed for the purpose of understanding more deeply the nonlinear flows, the authors chose not to belabor this point and hence the linear results for the more realistic value of E only are presented.

6.2 The Nonlinear Flow

The weakly nonlinear numerical results for $\epsilon = 5.8$ ($\Delta T = 0.5°C$) are shown in Figures 5. The flow is now, of course, much stronger and substantially different flow patterns are revealed when compared with the linearized results of Figures 4. The meridional flow is no longer a simple sidewall boundary layer flow, but takes the form of two vortices displaced towards the endwalls. The stronger meridional flow also penetrates further into the interior especially near the endwalls. The azimuthal flow is negative everywhere on the sidewall and has positive maxima in the interior. The isotherms reveal some slight distortion from the conduction solution (Fig. 3c) informing us that nonlinear temperature advection is becoming significant. Although the influence of rotation in confining this flow is clearly reduced, some confinement is still present.

Solutions of the strongly nonlinear flow for $\epsilon = 58$ ($\Delta T = 5°C$) are shown in Figures 6 and 7. The flow is rapid and unsteady. A weak oscillation is present and Figures 6 and 7 show extreme phases of the oscillation. The instantaneous flow is not symmetrical about mid-depth, but the time average is symmetrical. The oscillation period is about 0.4 sec. The meridional and azimuthal flows penetrate deeply into the interior. The maximum axial velocity fluctuates around 12.5 cm/sec and occurs on the sidewall. The maximum radial flow is inward; it fluctuates around 7.75 cm/sec and occurs near the corner regions. The conduction temperature solution (Fig. 3c) is severely distorted by the strong flow.

This flow is very nonlinear and the comments made in Subsection 4.2 about uniqueness are relevant. The flow presented in Figures 6 and 7 may not be unique and it is almost certainly unstable to azimuthal perturbations. Time dependent flows are believed to be the cause of dopant striations in crystals (see Section I) and theoretical and experimental studies of the stability of thermocapillary flows have been performed [17,18,19,20].

VII. CONCLUSIONS

For the model and parameter values chosen, the present work establishes that the thermocapillary flow is strong and that rotation cannot confine the flow. This conclusion is apparently reinforced by the fact that $\Delta T = 5°C$ could be considered too small and hence real flows are still stronger. However, an assessment of the results and the model reveals that actual flows may not be so strong and that rotation could still be used for confinement.

The distortion of the isotherms for the strongly nonlinear flow shown in Figures 6 and 7 reveals that temperature advection by the flow is significant even for the small Prandtl number ($Pr = 0.023$) of silicon. In the authors model the temperature on the sidewall was specified but, in fact, the actual temperature on the sidewall is determined by a balance of radiation, temperature advection, and conduction and since the results in this report show that temperature advection is important, a more realistic temperature boundary condition will be obtained by including all the processes. The inclusion of temperature advection will reduce the temperature gradient on the sidewall away from the endwalls and increase the temperature gradient close to the endwalls. This conclusion was also reached by Sen and Davis [19] who examined thermocapillary flow in a simpler configuration. Since the thermocapillary driving stress is now weaker over the bulk of the fluid and since viscosity may reduce the flow close to the endwalls, the overall nonlinear flow may be substantially reduced. A reduction in the flow strength will permit the confining effect of rotation to play a stronger role.

Since the melting point of silicon is about 1410°C, it is not unreasonable to think of $\Delta T = 5°C$ as somewhat small. However, since crystals have sharp melting points, the whole floating zone system could be placed in a furnace with a background temperature just below the melting point and only a small amount of heat from the ring heater would then be required to produce a floating zone [22,23]. This would result in a small ΔT and a corresponding weak flow. Surfactants will also reduce the surface tension stress [24,25] but, of course, suitable surfactants, which could not be considered as contaminants, would have to be used.

It is concluded that rotation may still be a means of confining the thermocapillary flow in a floating zone system to the melt sidewall. If this is so, then, in space, all flows in the melt interior will be greatly reduced. Further theoretical work and experimental confirmation of the theory is needed before this suggestion can be answered conclusively.

REFERENCES

1. Pimputkar, M. and Ostrach, S.: J. Crystal Growth, Vol. 55, 1981, p. 614.
2. Ostrach, S.: The 1982 Freeman Scholar Lecture. J. Fluids Engr, Vol. 105, 1983, p. 5.
3. Keller, W. and Muhlbauer, A.: Floating-Zone Silicon, Preparation and Properties of Solid State Materials, Vol. 5, 1981, Ed. L. R. Wilcox, Marcel Dekker, Inc.
4. Schwabe, D.: Physico-Chemical Hydrodynamics, Vol. 2, 1981, p. 263.
5. Chun, Ch.-H.: J. Crystal Growth, Vol. 45, 1980, p. 600.
6. Fu, B.-I. and Ostrach, S.: Report FTAS/TR-82-169, 1982, Case Western Reserve University.
7. Smith, M. K.: Accepted for publication in J. Fluid Mech.
8. Smith, M. K. and Greenspan, H. P.. Final Report, NASA MSFC Contract NAS8-35412, 1984.
9. Greenspan, H. P.: The Theory of Rotating Fluids, Cambridge University Press, 1969.
10. Kobayashi, N. and Wilcox, W. R.: J. Crystal Growth, Vol. 59, 1982, p. 616.
11. Giere, A. C. and Fowlis, W. W.: Geophys. Astrophys. Fluid Dynamics, Vol. 16, 1980, p. 207.
12. Fowlis, W. W. and Roberts, G. O.: Computational Methods and Experimental Measurements, Proceedings of the International Conference, Washington, D.C., July 1982, International Society for Computational Methods in Engineering, Springer-Verlag, New York.
13. Roberts, G. O., Fowlis, W. W., and Miller, T. L.: NASA Technical Paper 2323, 1984.
14. Warn-Varnas, A., Fowlis, W. W., Piacsek, S., and Lee, S. M.: J. Fluid Mech., Vol. 85, 1978, p. 609.
15. Hyun, J. M., Fowlis, W. W., and Warn-Varnas, A.: J. Fluid Mech., Vol. 117, 1982, p. 71.
16. Hyun, J. M., Leslie, F., Fowlis, W. W., and Warn-Varnas, A.: J. Fluid Mech., Vol. 127, 1983, p. 263.
17. Smith, M. K. and Davis, S. H.: J. Fluid Mech., Vol. 132, 1983, p. 119.
18. Smith, M. K. and Davis, S. H.: J. Fluid Mech., Vol. 132, 1983, p. 145.
19. Schwabe, D. and Scharmann, A.: J. Crystal Growth, 1979, p. 125.
20. Kamotani, Y., Ostrach, S., and Vargas, M.: J. Crystal Growth, Vol. 66, 1984, p. 83.
21. Sen, A. K. and Davis, S. H.: J. Fluid Mech., Vol. 121, 1982, p. 163.
22. Whitsett, C. R. and Nelson, D. A.: J. Crystal Growth, Vol. 6, 1969, p. 26.
23. Kern, E. L.: NASA MSFC Contract Report 170919, 1983.
24. Homsy, G. M. and Meiburg, E.: J. Fluid Mech., Vol. 139, 1984, p. 443.
25. Carpenter, B. and Homsy, G. M.: J. Fluid Mech., Vol. 155, 1985, p. 429.

APPENDIX A

THE LEADING ORDER $E^{1/3}$ SIDEWALL BOUNDARY LAYER

A transformation to the boundary layer scale was made using,

$$\xi = E^{-1/3}(A-r) \quad . \tag{A-1}$$

The velocity scale U was chosen to make $w_{1/3}$ of order unity. The amplitude scales are:

$$u_{1/3} = E^{1/3}\,\tilde{u}_{1/3} \;,\quad v_{1/3} = \tilde{v}_{1/3} \;,\quad w_{1/3} = \tilde{w}_{1/3} \;,\quad p_{1/3} = E^{1/3}\,\tilde{p}_{1/3} \;,\quad \psi_{1/3} = E^{1/3}\,\tilde{\psi}_{1/3} \;,$$

where the tilda denotes an 0(1) quantity. The scaled governing equations are,

$$2v_{1/3} = -\frac{\partial \tilde{p}_{1/3}}{\partial \xi} \quad , \tag{A-2}$$

$$\frac{\partial^2 \tilde{v}_{1/3}}{\partial \xi^2} - 2\tilde{u}_{1/3} = 0 \quad , \tag{A-3}$$

$$\frac{\partial^2 \tilde{w}_{1/3}}{\partial \xi^2} = \frac{\partial \tilde{p}_{1/3}}{\partial z} \quad , \tag{A-4}$$

$$-\frac{\partial \tilde{u}_{1/3}}{\partial \xi} + \frac{\partial \tilde{w}_{1/3}}{\partial z} = 0 \quad , \tag{A-5}$$

In terms of the stream function, one has,

$$\tilde{u}_{1/3} = \frac{\partial \tilde{\psi}_{1/3}}{\partial z} \quad , \quad \tilde{w}_{1/3} = \frac{\partial \tilde{\psi}_{1/3}}{\partial \xi} \quad . \tag{A-6}$$

The eliminated equation for $\tilde{\psi}_{1/3}$ is,

$$\frac{\partial^6 \tilde{\psi}_{1/3}}{\partial \xi^6} + 4\,\frac{\partial^2 \tilde{\psi}_{1/3}}{\partial z^2} = 0 \quad . \tag{A-7}$$

The boundary conditions on $\tilde{\psi}_{1/3}$ are:

$$\tilde{\psi}_{1/3} \rightarrow 0 \quad , \quad \text{as} \quad \xi \rightarrow \infty \quad , \tag{A-8}$$

$$\psi_{1/3} = \frac{\partial^2 \tilde{\psi}_{1/3}}{\partial \xi^2} + \sin \tfrac{1}{2} \pi z = \frac{\partial^5 \tilde{\psi}_{1/3}}{\partial \xi^5} = 0 \quad , \quad \text{on} \quad \xi = 0 \quad , \tag{A-9,a,b,c}$$

$$\tilde{\psi}_{1/3} = 0 \quad , \quad \text{or} \quad z = \pm 1 \quad . \tag{A-10}$$

The solutions are found using separation of variables. Sin ½ πz in equation (A-9b) is Fourier analyzed as,

$$\sin \tfrac{1}{2} \pi z = \sum_{n=1}^{\infty} a_n \sin n \pi z \quad , \tag{A-11}$$

where

$$a_n = (-1)^{n+1} \frac{2n}{\pi(n^2 - 1/4)} \quad .$$

Note that equation (A-11) is satisfied for all z in the domain $-1 \leqslant z \leqslant 1$ except $z = \pm 1$.

The solutions are:

$$\tilde{\psi}_{1/3} = \sum_{n=1}^{\infty} - \frac{a_n}{2\gamma_n^2} \left[e^{-\gamma_n \xi} + \frac{2}{3} e^{-\frac{1}{2}\gamma_n \xi} \sin\left(\frac{3}{2} \gamma_n \xi - \frac{2\pi}{3} \right) \right] \sin n\pi z \quad , \tag{A-12}$$

$$\tilde{v}_{1/3} = \sum_{n=1}^{\infty} - \frac{a_n}{2\gamma_n} \left[e^{-\gamma_n \xi} + \frac{2}{3} e^{-\frac{1}{2}\gamma_n \xi} \sin\left(\frac{3}{2} \gamma_n \xi \right) \right] \cos n\pi z \quad , \tag{A-13}$$

$$\tilde{w}_{1/3} = \sum_{n=1}^{\infty} \frac{a_n}{2\gamma_n} \left[e^{-\gamma_n \xi} - \frac{2}{3} e^{-\frac{1}{2}\gamma_n \xi} \sin\left(\frac{3}{2} \gamma_n \xi \right) \right] \sin n\pi z \quad , \tag{A-14}$$

$$\tilde{u}_{1/3} = \sum_{n=1}^{\infty} - \frac{a_n \gamma_n}{4} \left[e^{-\gamma_n \xi} + \frac{2}{3} e^{-\frac{1}{2}\gamma_n \xi} \sin\left(\frac{3}{2} \gamma_n \xi - \frac{2\pi}{3} \right) \right] \cos n\pi z \quad , \tag{A-15}$$

$$\tilde{p}_{1/3} = \sum_{n=1}^{\infty} - \frac{a_n}{\gamma_n^2} \left[e^{-\gamma_n \xi} - \frac{2}{3} e^{-\frac{1}{2}\gamma_n \xi} \sin\left(\frac{3}{2} \gamma_n \xi - \frac{2\pi}{3} \right) \right] \cos n\pi z \quad , \tag{A-16}$$

where $\gamma_n = (2n\pi)^{1/3}$. Note that all the boundary conditions, equations (A-8) through (A-10), and the symmetry conditions, equations (12) and (13) are satisfied, and also that the azimuthal stress, $\partial \tilde{v}_{1/3} / \partial \xi$, vanishes on $\xi = 0$.

APPENDIX B

THE EKMAN LAYERS ASSOCIATED WITH THE $E^{1/3}$ LAYER

A transformation to the boundary layer scale was made using,

$$\zeta = E^{-1/2}(1 - z) \quad . \tag{B-1}$$

Here only the Ekman layer near z = 1 is discussed. The Ekman layer near z = –1 is found by using $\zeta' = E^{-1/2}(1 + z)$. Using the Ekman layer to satisfy $v_{1/3} + v_{1/2} = 0$ at $z = 1$, the amplitude scales are determined as:

$$u_{1/2} = \tilde{u}_{1/2} \ , \ v_{1/2} = \tilde{v}_{1/2} \ , \ w_{1/2} = E^{1/6}\tilde{w}_{1/2} \ , \ p_{1/2} = E^{2/3}\tilde{p}_{1/2} \ , \ \psi_{1/2} = E^{1/2}\tilde{\psi}_{1/2} \quad .$$

The scaled governing equations are:

$$\frac{\partial^2 \tilde{u}_{1/2}}{\partial \zeta^2} + 2\tilde{v}_{1/2} = 0 \quad , \tag{B-2}$$

$$\frac{\partial^2 \tilde{v}_{1/2}}{\partial \zeta^2} - 2\tilde{u}_{1/2} = 0 \quad , \tag{B-3}$$

$$\frac{\partial^2 \tilde{w}_{1/2}}{\partial \zeta^2} = -\frac{\partial \tilde{p}_{1/2}}{\partial \zeta} \quad , \tag{B-4}$$

$$\frac{\partial \tilde{u}_{1/2}}{\partial \xi} + \frac{\partial \tilde{w}_{1/2}}{\partial \zeta} = 0 \quad . \tag{B-5}$$

The eliminated equation for $\tilde{u}_{1/2}$ or $\tilde{v}_{1/2}$ is,

$$\frac{\partial^4 \tilde{u}_{1/2}}{\partial \zeta^4} + 4\,\tilde{u}_{1/2} = 0 \quad . \tag{B-6}$$

The boundary conditions are:

All dependent quantities → 0 , as $\zeta \to \infty$, (B-7)

$$\tilde{u}_{1/2} = 0 \quad , \quad \text{on} \quad \zeta = 0 \quad , \tag{B-8}$$

$$\tilde{v}_{1/2} + \tilde{v}_{1/3} = 0 \quad , \quad \text{on} \quad \zeta = 0 \quad . \tag{B-9}$$

The solutions obtained are:

$$\tilde{\psi}_{1/2} = \frac{1}{2} V(\xi)\, e^{-\zeta} (\cos\zeta + \sin\zeta) \quad , \tag{B-10}$$

$$\tilde{v}_{1/2} = V(\xi)\, e^{-\zeta} \cos\zeta \quad , \tag{B-11}$$

$$\tilde{w}_{1/2} = \frac{1}{2} V'(\xi)\, e^{-\zeta} (\cos\zeta + \sin\zeta) \quad , \tag{B-12}$$

$$\tilde{u}_{1/2} = V(\xi)\, e^{-\zeta} \sin\zeta \quad , \tag{B-13}$$

$$\tilde{p}_{1/2} = V'(\xi)\, e^{-\zeta} \sin\zeta \quad , \tag{B-14}$$

where

$$V(\xi) = \sum_{n=1}^{\infty} (-1)^n \frac{a_n}{2\gamma_n} \left[e^{-\gamma_n \xi} + \frac{2}{3} e^{-\frac{1}{2}\gamma_n \xi} \sin\left(\frac{3}{2}\gamma_n \xi\right) \right]$$

and $V'(\xi)$ is its derivative with respect to ξ. Note that the boundary conditions [equations (B-7) through (B-9)] are satisfied. Note also that $\tilde{\psi}_{1/2}$ and $\tilde{w}_{1/2}$ are nonzero on $\zeta = 0$. The correct boundary conditions for these quantities are satisfied in conjunction with the first order $E^{1/3}$ layer. Note that $\tilde{u}_{1/2}$ is not equal to zero on $\xi = 0$. This point is discussed further in Section 6.

APPENDIX C

THE FIRST ORDER $E^{1/3}$ SIDEWALL BOUNDARY LAYER

Recalling the amplitude scales for the leading order problem and our boundary layer requirement that, $w_{1/3} \sim E^{1/6}$, the dependent quantities are expanded as follows:

$$u_{1/3} = E^{1/3} (\tilde{u}_{1/3} + E^{1/6} \, {}_1\tilde{u}_{1/3} + \ldots) \ , \tag{C-1}$$

$$v_{1/3} = \tilde{v}_{1/3} + E^{1/6} \, {}_1\tilde{v}_{1/3} + \cdots \ , \tag{C-2}$$

$$w_{1/3} = \tilde{w}_{1/3} + E^{1/6} \, {}_1\tilde{w}_{1/3} + \cdots \ , \tag{C-3}$$

$$p_{1/3} = E^{1/3} (\tilde{p}_{1/3} + E^{1/6} \, {}_1\tilde{p}_{1/3} + \ldots) \ , \tag{C-4}$$

$$\psi_{1/3} = E^{1/3} (\tilde{\psi}_{1/3} + E^{1/6} \, {}_1\tilde{\psi}_{1/3} + \ldots) \ . \tag{C-5}$$

Using this sidewall layer to match the Ekman layer $w_{1/2} \sim E^{1/6}$, one obtains for the amplitude scales.

$${}_1u_{1/3} = E^{1/2} \, {}_1\tilde{u}_{1/3} \ , \ {}_1v_{1/3} = E^{1/6} \, {}_1\tilde{v}_{1/3} \ , \ {}_1w_{1/3} = E^{1/6} \, {}_1\tilde{w}_{1/3} \ , \ {}_1p_{1/3} = E^{1/2} \, {}_1\tilde{p}_{1/3} \ ,$$

$${}_1\psi_{1/3} = E^{1/2} \, {}_1\tilde{\psi}_{1/3} \ .$$

The scaled governing equations are identical to those of the leading order problem, namely,

$$2 \, {}_1\tilde{v}_{1/3} = - \frac{\partial \, {}_1\tilde{p}_{1/3}}{\partial \xi} \ , \tag{C-6}$$

$$\frac{\partial^2 \, {}_1\tilde{v}_{1/3}}{\partial \xi^2} - 2 \, {}_1\tilde{u}_{1/3} = 0 \ , \tag{C-7}$$

$$\frac{\partial^2 \, {}_1\tilde{w}_{1/3}}{\partial \xi^2} = \frac{\partial \, {}_1\tilde{p}_{1/3}}{\partial z} \ , \tag{C-8}$$

$$-\frac{\partial_1 \tilde{u}_{1/3}}{\partial \xi} + \frac{\partial_1 \tilde{w}_{1/3}}{\partial z} = 0 \quad . \tag{C-9}$$

The stream function is written as,

$${}_1\tilde{u}_{1/3} = \frac{\partial_1 \tilde{\psi}_{1/3}}{\partial z} \quad , \quad {}_1\tilde{w}_{1/3} = \frac{\partial_1 \tilde{\psi}_{1/3}}{\partial \xi} \quad . \tag{C-10}$$

The eliminated equation for ${}_1\tilde{\psi}_{1/3}$ is,

$$\frac{\partial^6 {}_1\tilde{\psi}_{1/3}}{\partial \xi^6} + 4\frac{\partial^2 {}_1\psi_{1/3}}{\partial z^2} = 0 \quad . \tag{C-11}$$

The boundary conditions for ${}_1\tilde{\psi}_{1/3}$ are:

$${}_1\tilde{\psi}_{1/3} \to 0 \quad , \quad \text{as } \xi \to \infty \quad , \tag{C-12}$$

$${}_1\hat{\psi}_{1/3} = \frac{\partial^2 {}_1\tilde{\psi}_{1/3}}{\partial \xi^2} = \frac{\partial^5 {}_1\tilde{\psi}_{1/3}}{\partial \xi^5} = 0 \quad , \quad \text{on } \xi = 0 \quad , \tag{C-13}$$

$${}_1\tilde{\psi}_{1/3} = \pm\frac{1}{2}\tilde{v}_{1/3} = \pm\frac{1}{2}V(\xi) \quad , \quad \text{on } \; z = \pm 1 \quad , \tag{C-14}$$

where

$$V(\xi) = \sum_{n=1}^{\infty} (-1)^n \frac{a_n}{2\gamma_n}\left[e^{-\gamma_n \xi} + \frac{2}{3}e^{-\frac{1}{2}\gamma_n \xi}\sin\left(\frac{3}{2}\gamma_n \xi\right)\right]$$

as before. Solutions of the above equations and boundary conditions are not given.

APPENDIX D

THE $E^{1/4}$ SIDEWALL BOUNDARY LAYER AND ITS ASSOCIATED EKMAN LAYER

A transformation to the boundary layer scale was made using,

$$\eta = E^{-1/4}(A - r) \quad . \tag{D-1}$$

To take care of the sidewall azimuthal stress introduced by the first order $E^{1/3}$ sidewall layer, $v_{1/4} \sim 0(E^{1/12})$ is required and the amplitude scales are then determined as.

$$u_{1/4} = E^{7/12}\tilde{u}_{1/4} \ , \ v_{1/4} = E^{1/12}\tilde{v}_{1/4} \ , \ w_{1/4} = E^{1/3}\tilde{w}_{1/4} \ , \ p_{1/4} = E^{1/3}\tilde{p}_{1/4} \ ,$$

$$\psi_{1/4} = E^{7/12}\tilde{\psi}_{1/4} \ .$$

The scaled governing equations are:

$$2\tilde{v}_{1/4} = -\frac{\partial \tilde{p}_{1/4}}{\partial \eta} \quad , \tag{D-2}$$

$$\frac{\partial^2 \tilde{v}_{1/4}}{\partial \eta^2} - 2\tilde{u}_{1/4} = 0 \quad , \tag{D-3}$$

$$\frac{\partial \tilde{p}_{1/4}}{\partial z} = 0 \quad , \tag{D-4}$$

$$-\frac{\partial \tilde{u}_{1/4}}{\partial \eta} + \frac{\partial \tilde{w}_{1/4}}{\partial z} = 0 \quad . \tag{D-5}$$

The stream function is written as,

$$\tilde{u}_{1/4} = \frac{\partial \tilde{\psi}_{1/4}}{\partial z} \quad , \quad \tilde{w}_{1/4} = \frac{\partial \tilde{\psi}_{1/4}}{\partial \eta} \quad . \tag{D-6}$$

From equations (D-2) through (D-6) one deduces,

$$\frac{\partial \tilde{u}_{1/4}}{\partial z} = \frac{\partial \tilde{v}_{1/4}}{\partial \xi} = \frac{\partial \tilde{p}_{1/4}}{\partial z} = \frac{\partial^2 \tilde{w}_{1/4}}{\partial z^2} = \frac{\partial^2 \tilde{\psi}_{1/4}}{\partial z^2} = 0 \quad . \tag{D-7a,b,c,d,e}$$

One clearly has an Ekman layer associated with this $E^{1/4}$ layer. Scaling for this Ekman layer to make $v_{1/4} + v_{1/2} = 0$ on $z = \pm 1$, yields:

$$u_{1/2} = E^{1/12}\tilde{u}_{1/2} \ , \ v_{1/2} = E^{1/12}\tilde{v}_{1/2} \ , \ w_{1/2} = E^{1/3}\tilde{w}_{1/2} \ , \ p = E^{5/6}\tilde{p}_{1/2} \ , \ \psi_{1/2} = E^{7/12}\tilde{\psi}_{1/2} \, .$$

Ekman compatibility yields,

$$\tilde{w}_{1/4} = \pm \frac{1}{2} \frac{\partial \tilde{v}_{1/4}}{\partial \eta} \quad , \text{ on } z = \pm 1 \quad . \tag{D-8}$$

Equation (26) gives the azimuthal sidewall stress and let this stress equal S, i.e.,

$$\frac{\partial \tilde{v}_{1/4}}{\partial \eta} = \sum_{n=1}^{\infty} (-1)^{n+1} \frac{a_n}{\gamma_n^{\,2}} = S \quad , \text{ on } \eta = 0 \quad . \tag{D-9}$$

Remembering that the problem is symmetric about z = 0 and using the above equations and boundary conditions, the solutions are found to be.

$$\psi_{1/4} = -\frac{1}{2} S e^{-\eta} z \quad , \tag{D-10}$$

$$\tilde{v}_{1/4} = - S e^{-\eta} \quad , \tag{D-11}$$

$$\tilde{w}_{1/4} = \frac{1}{2} S e^{-\eta} z \quad , \tag{D-12}$$

$$\tilde{u}_{1/4} = -\frac{1}{2} S e^{-\eta} \quad , \tag{D-13}$$

$$\tilde{p}_{1/4} = - 2 S e^{-\eta} \quad . \tag{D-14}$$

Note that the azimuthal sidewall stress condition is satisfied but $\tilde{\psi}_{1/4}$ and $\tilde{u}_{1/4}$ are not equal to zero on $\eta = 0$.

The Ekman layer solutions are found as before for the $E^{1/3}$ layer (see Appendix B). The leading order boundary conditions are:

$$\left.\begin{aligned}&\tilde{u}_{1/2}=0 \quad , &&(\text{D-15})\\ &\tilde{v}_{1/2}+\tilde{v}_{1/4}=0 \quad . &&(\text{D-16})\end{aligned}\right\} \quad \text{on } \zeta=0$$

The solutions are:

$$\tilde{\psi}_{1/2}=\frac{1}{2}\,Se^{-\eta}\,e^{-\zeta}\,(\sin\zeta+\cos\zeta) \quad , \tag{D-17}$$

$$\tilde{v}_{1/2}=Se^{-\eta}\,e^{-\zeta}\cos\zeta \quad , \tag{D-18}$$

$$\tilde{w}_{1/2}=-\frac{1}{2}\,Se^{-\eta}\,e^{-\zeta}\,(\sin\zeta+\cos\zeta) \quad , \tag{D-19}$$

$$\tilde{u}_{1/2}=Se^{-\eta}\,e^{-\zeta}\sin\zeta \quad , \tag{D-20}$$

$$\tilde{p}_{1/2}=Se^{-\eta}\,e^{-\zeta}\sin\zeta \quad . \tag{D-21}$$

These Ekman layer solutions rigorously satisfy the $E^{1/4}$ layer endwall boundary conditions.

APPENDIX E

THE NUMERICAL CODE

The code solves the Boussinesq form of the axisymmetric, incompressible, Navier-Stokes equations in the configuration of Figure 2. Finite difference methods are used. To give adequate resolution in the boundary layers without wasting resolution in the interior, a nonuniform computational mesh is specified. The dependent variables are represented by their values at the same primary mesh points, which simplifies part of the coding and allows for the efficient use of implicit methods. The spatial representation conserves several integral quantities.

An iterative method based on time-stepping is used to obtain steady solutions. This method has the option of different time steps for temperature and velocity and these steps vary smoothly according to specified powers of the mesh spacing in the two directions. This permits more rapid convergence to steady states than simple uniform time-stepping. An alternating-direction implicit formulation is used for advection and diffusion and for the Coriolis force, with implicit parameters chosen to damp high frequency phenomena.

The pressure field is determined from the continuity equation. The total pressure at the previous iteration is used as a first approximation to update the velocity variables. The velocity divergence is then calculated and used to obtain a convection pressure field which is then used to correct the velocities. This convection pressure satisfies a representation of a Poisson-like equation, which is solved by alternating direction implicit iteration.

1. REPORT NO.
NASA TP-2576

2. GOVERNMENT ACCESSION NO.

3. RECIPIENT'S CATALOG NO.

4. TITLE AND SUBTITLE
Analytical and Numerical Studies of the Thermocapillary Flow in a Uniformly Rotating Floating Zone

5. REPORT DATE
March 1986

6. PERFORMING ORGANIZATION CODE

7. AUTHOR(S)
William W. Fowlis and Glyn O. Roberts*

8. PERFORMING ORGANIZATION REPORT #

9. PERFORMING ORGANIZATION NAME AND ADDRESS

George C. Marshall Space Flight Center
Marshall Space Flight Center, Alabama 35812

10. WORK UNIT NO.
M-518

11. CONTRACT OR GRANT NO.

12. SPONSORING AGENCY NAME AND ADDRESS

National Aeronautics and Space Administration
Washington, D.C. 20546

13. TYPE OF REPORT & PERIOD COVERED

Technical Paper

14. SPONSORING AGENCY CODE

15. SUPPLEMENTARY NOTES
Prepared by Space Science Laboratory, Science Engineering Directorate.

*Roberts Associates, Inc., Vienna, Virginia 22180.

16. ABSTRACT

The microgravity environment of an orbiting vehicle permits crystal growth experiments in the presence of greatly reduced buoyant convection in the liquid melt. Crystals grown in ground-based laboratories do not achieve their potential properties because of dopant variations caused by flow in the melt. The floating zone crystal growing system is widely used to produce crystals of silicon and other materials. However, in this system the temperature gradient on the free sidewall surface of the melt is the source of a thermocapillary flow which does not disappear in the low-gravity environment.

Smith and Greenspan theoretically examined the idea of using a uniform rotation of the floating zone system to confine the thermocapillary flow to the melt sidewall leaving the interior of the melt passive. These workers considered a cylinder of fluid with an axial temperature gradient imposed on the cylindrical sidewall. They considered a half zone and examined the linearized, axisymmetric flow in the absence of crystal growth. They found that rotation does confine the linear thermocapillary flow.

In this paper the simplified model of Smith and Greenspan is extended to a full zone and both linear and nonlinear thermocapillary flows are studied theoretically. Analytical and numerical methods are used for the linear flows and numerical methods for the nonlinear flows. It was found that the linear flows in the full zone have more complicated and thicker boundary layer structures than in the half zone, and that these flows are also confined by the rotation. However, for the simplified model considered and for realistic values for silicon, the thermocapillary flow is not linear. The nonlinear flows were examined by first computing a weakly nonlinear flow and then computing the fully nonlinear flow. The weakly nonlinear flow is steady, has less boundary layer character, and penetrates more deeply into the interior than the linear flow but still shows some rotational confinement. The fully nonlinear flow is strong and unsteady (a weak oscillation is present) and it penetrates the interior. Some non-rotating flow results are also presented.

Since silicon has a large value of thermal conductivity, one would expect the temperature fields to be determined by conduction alone. This is true for the linear and weakly nonlinear flows, but for the stronger nonlinear flow the results show that temperature advection is also important. Thus, this work reveals that for the nonlinear flow, a radiative sidewall boundary condition would be an improvement over the specified temperature boundary condition used in this paper and previously by others. Such a boundary condition would weaken the sidewall axial temperature gradient and hence the thermocapillary flow allowing the confining effect of rotation to play a stronger role. Hence, uniform rotation may still be a means of confining the flow and the results obtained define the procedure to be used to examine this hypothesis.

17. KEY WORDS

Floating Zone
Theoretical Thermocapillary Flow Studies
Confinement of Thermocapillary by Rotation

18. DISTRIBUTION STATEMENT

Unclassified – Unlimited

Subject Category 34

19. SECURITY CLASSIF. (of this report)
Unclassified

20. SECURITY CLASSIF. (of this page)
Unclassified

21. NO. OF PAGES
41

22. PRICE
A03

For sale by National Technical Information Service, Springfield, Virginia 22161
NASA-Langley, 1986

National Aeronautics and
Space Administration
Code NIT-4

Washington, D.C.
20546-0001

Official Business
Penalty for Private Use, $300

BULK RATE
POSTAGE & FEES PAID
NASA
Permit No. G-27

NASA

POSTMASTER: If Undeliverable (Section 158
Postal Manual) Do Not Return